REVIEWS OF TOPICAL PROBLEMS

40th ANNIVERSARY OF THE PROKHOROV GENERAL PHYSICS INSTITUTE,
RUSSIAN ACADEMY OF SCIENCES

Acoustic properties of the sea bottom and their effect on long-range sound propagation on the Arctic shelf

A A Lunkov, V A Grigorev, V G Petnikov

Contents

Abstract. The results of a study of the long-range propagation of low-frequency acoustic waves in shallow water over distances much greater than the water depth are presented. The primary focus is on the characteristics of the sound fields due to the influence of an inhomogeneous seabed. The effect of the physical properties of the bottom on the attenuation and refraction of acoustic waves is given special attention. Emphasis is placed on sound propagation on the Arctic shelf, where the inhomogeneities in the upper layer of the bottom sediments are particularly pronounced. Examples of the inhomogeneities obtained from 3D seismic surveys and shallow seabed drilling are given.

Keywords: shallow water acoustics, waveguide with random inhomogeneities

A A Lunkov [(1, a)], **V A Grigorev** [(1, 2, b)], **V G Petnikov** [(1, c)]
[(1)] Prokhorov General Physics Institute, Russian Academy of Sciences,
 ul. Vavilova 38, 119991 Moscow, Russian Federation
[(2)] Voronezh State University,
 Universitetskaya pl. 1, 394018 Voronezh, Russian Federation
E-mail: [(a)] lunkov@kapella.gpi.ru, [(b)] grig4@yandex.ru,
 [(c)] petniko@kapella.gpi.ru

1. Introduction

The term 'shallow water' appeared in underwater acoustics a long time ago and is mainly associated with studies of the long-range propagation ($r \gg H$, where r is the distance and H is the depth) of low-frequency acoustic waves (less than 1 kHz) on the ocean shelf [1, 2]. Sound propagation in a shallow water has a waveguide character, with the sea surface and the seabed being the waveguide boundaries. Using the ray language, one can say that the sound field at large distances is mainly formed by rays reflected many times from the seabed. In this respect, a principal difference between a shallow water and a deep ocean is the significant influence of the bottom, and mainly its upper sediment layer, on the formation of the sound field. A good illustration of this statement is paper [3], which demonstrates the sensitivity of transmission loss to a variation in the parameters of the upper sediment layer in the Shallow Water 2006 experiment carried out on the US Atlantic shelf.

The effect of the bottom is most evident on the Arctic shelf. This is confirmed, for example, by the strong spatial sound attenuation in a near-bottom sound channel (an acoustic waveguide formed by the bottom and the sea surface) measured in experiments carried out by the Prokhorov General Physics Institute (GPI RAS). The experiments were conducted in seven different regions of the Barents Sea on acoustical tracks up to 400 km long. The tracks were located in the southern part of the area which was

explored. Signals were emitted by towed quasi-point sound sources, and a vertical array of hydrophones, crossing a significant part of the waveguide, was used as a receiver. The coefficient of sound field attenuation was calculated as the tangent of the slope angle of the experimental logarithmic dependence of sound intensity $\bar{\delta}(r, z)$ on distance r for receiver depth z. (The bar indicates spatial averaging over an interval exceeding the spatial period of the interference beat. The reduction in wave intensity due to geometrical divergence of the sound wave front was excluded from consideration.) The technique used to estimate the attenuation coefficient is described in more detail in [4]. The results of the measurements for each track and for different receiver depths were averaged over the depth. The mean value of the attenuation coefficient on these paths was found to be[1] $\bar{\beta} = 0.106 \pm 0.057$ dB km^{-1} at a frequency of 100 Hz, which is at least an order of magnitude higher than the values found in the deep ocean where sound does not interact with the seafloor.

We note here a rather large confidence interval for the values of $\bar{\beta}$ which, as shown by additional simulations, cannot be caused by varying depth in the area or by different vertical sound speed profiles in water on the explored acoustic tracks. (The simulation technique is described below.) Most likely, the cause lies in quasi-random seafloor inhomogeneities with different acoustic properties and different horizontal and vertical spatial scales. This hypothesis is indirectly confirmed by the distribution of density in the upper (0–5 m) sediment layer, as measured in bottom sediment samples in the Barents Sea taken by the P P Shirshov Institute of Oceanology RAN with geological tubes at the step of ≈ 30 km [5] (Fig. 1). This distribution, with significant density variations between sampling points, was obtained along a straight line cutting the central Barents Sea from its southern to northern boundaries.

It should be noted that strong spatial variability in ocean bottom characteristics is present everywhere on the ocean shelf (see, e.g., [6]). The Arctic shelf has its own specific features, partly related to natural gas seeps from deep layers [7]. As a result, based on low-frequency seismic profiling, the observed features in the northern seas of Russia are:
• layered sedimentary regions up to tens of kilometers in length, including wedge-shaped layers;
• narrow vertical channels formed by natural gas seeps, with pockmarks (craters) at the water–bottom interface;
• diapiric structures (dome-shaped folds formed by natural gas pushing high-plasticity bottom layers upward from below);
• paleovalleys of rivers filled with material that is different from the surrounding material.

In addition, as shown by recent geophysical studies [8, 9], the observed features are alternating regions of frozen, thawed (multi-year cooled), and gas-saturated bottom [10], where the physical parameters in the upper sediment layer — sound speed, density, and sound attenuation coefficient — vary over a wide range.

From the point of view of physical acoustics, the upper sediment layer thus represents a medium characterized by a random spatially distributed specific acoustic impedance (wave resistance) $Z_1 = c_1 \rho_1 / (1 + i \alpha_1 / 2)$, where c_1, ρ_1, and α_1 are the local values of the sound speed, density, and loss parameter defining the imaginary part of the wavenumber k_1
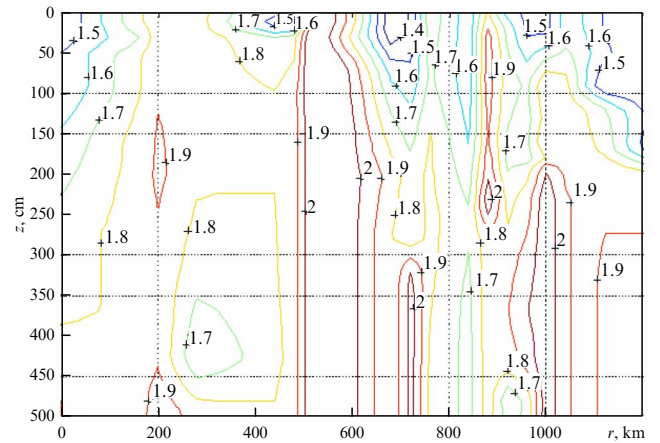
Figure 1. Distribution of density (g cm^{-3}) in the upper sediment layer in the Barents Sea. Colored lines are density isolines.
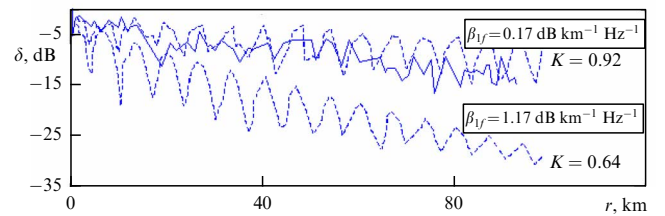
Figure 2. Experimental (solid) and simulated (dashed) dependences of $\delta(r, z)$ for different values of the sound attenuation coefficient in the sea bottom β_{1f}.

---

in the seabed, respectively ($k_1 = \omega(1 + i \alpha_1 / 2) / c_1$, where ω is the sound frequency). Unfortunately, the randomly inhomogeneous spatial fields of the physical quantities c_1, ρ_1, and α_1 are, as a rule, unknown. As a consequence, in shallow water acoustics, it is often assumed that the seafloor is a homogeneous liquid medium with some constant effective parameters: sound speed c_1^{eff}, density ρ_1^{eff}, and parameter of loss α_1^{eff} (see [2] and references therein). The effective parameters are usually chosen so that the experimental δ_{e} and simulated δ_{th} curves of the sound field attenuation

$$\delta_{\mathrm{e, th}}(r, z) = 10 \lg \frac{I_{\mathrm{e, th}}(r, z)}{I_{\mathrm{e, th}}(r_0, z)} + 10 \lg \frac{r}{r_0} \qquad (1)$$

are as close as possible to each other. Here, $I_{\mathrm{e, th}}(r, z)$ is the sound field intensity (experimental and simulated with "e" is for experimental, "th" is for simulated) at the horizontal distance r from the sound source and at the depth z, and r_0 is the initial distance usually chosen so as to make this technique adequate.

We look at this method of choosing the seabed parameters in more detail, using the studies carried out by GPI RAS in the Barents Sea (Fig. 2). Here, the sound frequency was $f = \omega / 2\pi = 100$ Hz. The distance r_0 was taken to be 0.5 km. The water column depth was $H \approx 230$ m. The depths of the source z_0 and the receiver z were $z_0 = 40$ m and $z = 65$ m. The bottom sound attenuation coefficient $\beta_{1f} = 27.3 \alpha_1 / c_1$ [dB (km Hz)$^{-1}$] was the effective parameter that was determined. It should be noted that this coefficient is characterized by the largest uncertainty compared to other seabed parameters: sound speed c_1 and density ρ_1. The degree of closeness

between the experimental and calculated attenuation curves in Fig. 2 was estimated using the following criterion:

$$K = \bar{K} + \tilde{K}, \qquad \delta_{e,th} = \bar{\delta}_{e,th} + \tilde{\delta}_{e,th},$$

$$\bar{K} = \frac{\int_0^r \bar{\delta}_e \bar{\delta}_{th}\, dr}{\int_0^r \bar{\delta}_e^2\, dr + \int_0^r \bar{\delta}_{th}^2\, dr}, \quad \tilde{K} = \frac{\int_0^r \tilde{\delta}_e \tilde{\delta}_{th}\, dr}{\int_0^r \tilde{\delta}_e^2\, dr + \int_0^r \tilde{\delta}_{th}^2\, dr}, \quad (2)$$

where $\bar{\delta}_{e,th}$ corresponds to the sound field intensity $\langle I \rangle$ averaged over the longitudinal length greater than the maximum horizontal scale of the interference beat, and $\tilde{\delta}_{e,th}$ corresponds to the fluctuating part of the intensity $\tilde{I} = I - \langle I \rangle$. The value of K close to one corresponds to the best agreement between the experiment and the simulations. As can be seen from Fig. 2, the experimental and calculated dependences are closest to each other ($K = 0.92$) for $\beta_{1f} = 0.167$ [dB (km Hz)$^{-1}$]. This value was taken as the effective one. In the simulations, it was assumed that $c_1 = 1630$ m s^{-1} and $\rho_1 = 2$ g cm^{-3}.

Another well-known approach is to treat the seabed as a consolidated or unconsolidated sediment layer lying on an elastic half-space (see, e.g., [2, 11–14]). In this case, the efficient parameters include additionally the density ρ_2^{eff} and the propagation speeds c_2^{eff} and c_{2s}^{eff} of the longitudinal and transverse waves in the half-space, as well as the speed of transverse waves in the layer c_{1s}^{eff} if it is considered to be consolidated. Some studies deal with even more complex models with several layers above the half-space, and select effective parameters for each layer [15–17]. In all such models, the values of the above parameters are commonly chosen to give approximately the same sound attenuation in the water layer for waveguide propagation as for the real randomly inhomogeneous bottom.

The quantities c_1 and ρ_1 vary practically randomly within a shallow water region. Their statistical distributions are different in different shallow waters, and it is likely that these random fields have the largest variance for the Arctic shelf. In this region, the spatial variability scales of these quantities are not large, less than about 10 km on average. At the present time, with advances in speed analysis techniques for 3D seismic survey data, it has become possible to measure the dependence of sound speed c_1 on spatial coordinates for given regions on the ocean shelf. (The methodology of such measurements using reflected waves is presented, for example, in [18–20].) When seismic surveys are also accompanied by bottom drilling with material sampling and density measurements, new tasks in shallow-sea acoustics become possible in the study of acoustic wave propagation in shallow regions where the bottom impedance is approximately known and varies in some way along the sound propagation track. One such task worth mentioning first of all is the comparative estimation of sound field attenuation in the water layer for different distances from the source and different propagation directions, i.e., for acoustic tracks over the sea floor with significantly different and variable impedance. The problem of comparing the real mean sound speed in the bottom with the effective sound speed also arises here.

A special case in these tasks is when $c_1 \approx c$, where c is the sound speed in the water layer. Such a bottom is called water-like.

Knowledge of impedance variations with high spatial resolution allows estimates of the horizontal refraction of sound waves caused by variations in the seabed acoustic properties. What is of interest are the variations in the direction transverse to the wave propagation. The effects of horizontal sound refraction in the ocean were studied for a sufficiently long time. The first theoretical studies on this subject were carried out in the 1980s [21, 22]. The results of experimental observations can be found, for example, in [23–25]; however, in all these studies, the refraction was caused either by transverse changes in the waveguide depth or by hydrodynamical perturbations in the water column (internal waves, mesoscale eddies, etc.). Only Ref. [26] mentioned variations in seabed properties as a cause of horizontal refraction. Here, this wave phenomenon was studied on the shallow US Atlantic shelf, which is also characterized by transverse depth variations, which in the end were the main cause of horizontal refraction.

In contrast to the US Atlantic shelf, most of the regions of the Russian Arctic shelf are characterized by smooth depth variability. For example, in the above-mentioned studies carried out by the GPI RAS in the Barents Sea, the depth gradient did not exceed $\Delta H / \Delta r \leqslant 10^{-3}$. In such circumstances, horizontal refraction caused solely by changes in seabed properties can be seen well.

This review extends and generalizes the results of studies of low-frequency acoustical fields on the Arctic shelf in regions with almost constant depth but a spatially inhomogeneous bottom, within one and the same framework. The bottom characteristics (its sound speed and sometimes density) are known and were obtained as a result of geophysical studies. The main focus is placed on estimates of sound field intensity at distances from sound sources that are much larger than the waveguide depth. We also include a case when the sound field amplitude depends not only on sound attenuation along a straight line between the source and receiver but also on the degree to which a sound ray deviates from this line due to horizontal refraction. These studies were carried out at the GPI RAS. The data from 3D seismic surveys, drilling, and numerical modeling are utilized (see Refs [27–31] for details).

The simulations are based on a modal description of the sound field. We need to provide details of methodological approximations that are used. Specifically, the analysis of speeds in 3D seismic surveys does not provide estimates of the quantity α_1 which defines the attenuation of sound waves in seabed sediment matter. Therefore, the sound attenuation coefficient in a seabed $\beta_{1f} = 27.3\alpha_1/c_1$ was chosen based on the published data, which, in turn, show a substantial scatter in possible values. Here, it is assumed that the coefficient does not vary with spatial coordinates but varies with frequency: $\beta_{1f} = 1.07 \times 10^{-4} f^{1.6}$ [dB (km Hz)$^{-1}$] [32], where f is the frequency in Hz. The factor 1.07×10^{-4} was chosen so as to reproduce typical attenuation values in the range of 100–250 Hz in the shallow eastern part of the Barents Sea found in experiments carried out by the GPI RAS (see above). The available results of test drilling in this region were also insufficient to assess the spatial distribution of seabed density ρ_1. The value of ρ_1 used in simulations was kept constant and set to the mean value of seabed density obtained from drilling.

It should be stressed that all simulations were conducted assuming a constant sound speed c in seawater and the absence of the sea ice cover, which was the case during the seismic survey (the period of summer and fall). The value of c can certainly depend on the depth z, and it is known that the gradient of vertical sound speed profile $c(z)$ shows seasonal variability ranging from significant negative values in

summer to positive values in winter. The simulated results are quantitatively dependent on the selected profile of $c(z)$; however, as follows from additional simulations, they do not change qualitatively. In this review, we present only the results for $c(z) = \mathrm{const}$. These results, on the one hand, reflect some 'average' situation for a shallow (depth $H \leqslant 30$ m) Arctic shelf, and on the other hand, correspond to a typical situation.[2] Therefore, we intend to draw the reader's attention to the seabed influence on sound propagation.

Sound propagation was considered at moderate distances (up to 10 km) and at low frequencies (up to 1 kHz). This selection was motivated by concern for protecting marine mammals from intense anthropogenic acoustical noise. Intense acoustical noise with the specified parameters is commonly produced in seismic prospecting for hydrocarbons. Foreseeing noise intensity is necessary to aid protection.

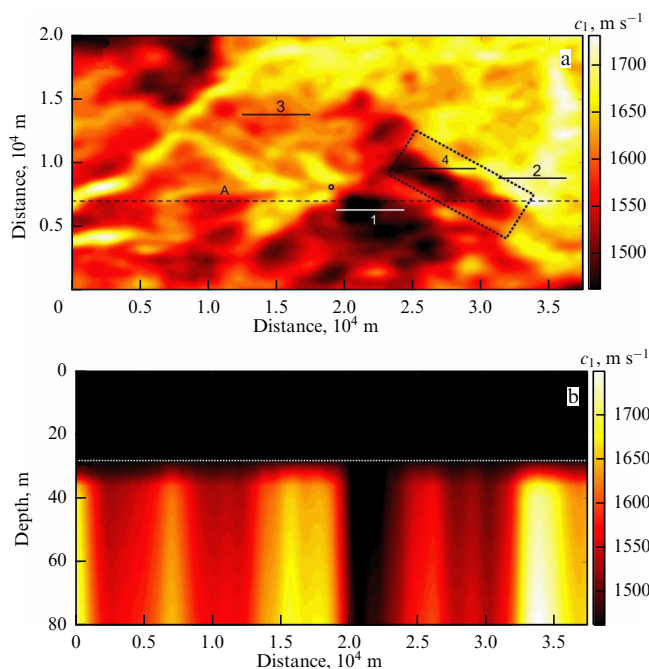## 2. Example of bottom structure on the Arctic shelf

In this section, as an example, we present results of 3D seismic surveys and sample drilling in a region of the Kara Sea, as described in [27]. The data includes the field of sound speed in the bottom as a function of Cartesian coordinates $c_1(x, y, z)$, where the coordinate origin is taken on the sea surface, and the z-axis is directed vertically downward. The resolution along the z-axis is 4 m, and the resolution along the x-axis and y-axis is 100 m on average. As an illustration, Fig. 3 shows transects of the sound speed field: horizontal and vertical (along line A), which allow an assessment of the degree of inhomogeneity of bottom sediments. The transect in Fig. 3a was taken in the bottom at a depth of 51 m, for a sea depth of 25–50 m. In the transect in Fig. 3b, the water–bottom interface is at an approximately constant depth of ≈ 28 m (horizontal dashed line in Fig. 3b).

In Fig. 3, one can see dark regions at the bottom, which are oriented nearly vertically in Fig. 3b. These are the regions of water-like bottom where the sound speed is close to that in water ($c = 1460$ m s^{-1}), which are related to gas seeps from deep layers. Figure 3b also clearly illustrates a transitional layer along the bottom surface with a width of 10 m, covering the entire bottom from above, in which the sound speed ranges from values similar to those in water to values found in deep layers.

The low-speed transitional layer in the upper part of the bottom sediment layer, where no deep gas seeps are observed, can be caused by two factors: (1) the presence of gas formed via decomposition of local organic matter and also the presence of cryogenic gas; (2) the presence of silty, water-saturated sediments, in which, as is well known, the sound speed is close to that in water.

To analyze these factors, consider Fig. 4, which presents a comparison of the profiles of the sound speed and seabed density on the same vertical line. The horizontal coordinates of this line are shown in Fig. 3a by a circle. Figure 4a shows the sound speed profile averaged over the scales $\Delta x \, \Delta y \, \Delta z = 100 \times 100 \times 4$ m. The solid bold line in Fig. 4b shows the mean density profile down to a depth of 40 m taking into account the confidence interval (the region with a significance
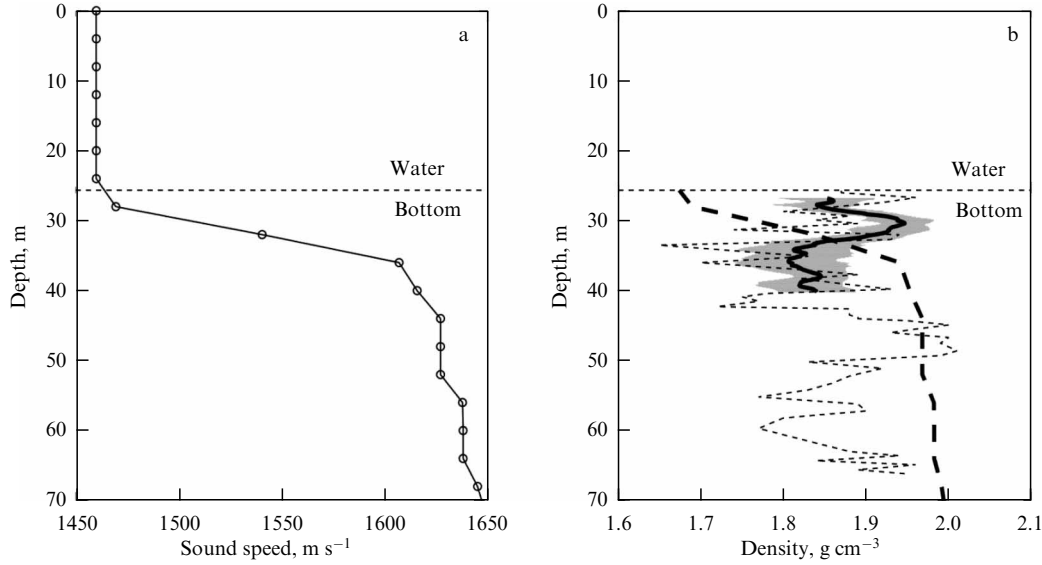

Figure 3. (a) Horizontal and (b) vertical (along line A) sections of the sound speed in the bottom obtained in 3D seismic surveys in the Kara Sea. Horizontal dashed line in panel b shows the water–bottom interface. Intervals numbered 1–4 in panel a show acoustical tracks used to analyze sound propagation. Dotted rectangle marks the region where mode coupling and horizontal sound refraction were studied.

of 0.95 by the Student's criterion is shaded gray). The density was measured by taking samples from 16 boreholes drilled in the seabed and located approximately uniformly in a square 300×300 m in size. (The center of the square coincides with the center of the circle in Fig. 3a.) The total number of samples was 358. The size of each sample was $10 \times 10 \times 10$ cm, and the step in the vertical direction was varied in the range of $0.2 - 2.2$ m, with a mean step of 0.8 m. One borehole was drilled down to a depth of 65 m. The density data from this borehole are displayed in Fig. 4b by a thin dashed line.

The bold dashed line in Fig. 4b shows a theoretical density profile calculated from the sound speed profile (Fig. 4a) under the assumption that there is no gas in the bottom material. The calculations were based on the empirical formulas of Akal [33], which represents a generalization of observational data over the entire global ocean: $c_1 = c(1.631 - 1.78\kappa + 1.2\kappa^2)$, $\rho_1 = \rho(2.604 - 1.606\kappa)$, where $c = 1460$ m s^{-1}, $\rho = 1$ g cm^{-3} are the sound speed in water and water density near the bottom, respectively, and κ is the bottom porosity. Note that the Akal formulas agree well with the analytical expressions for a two-component medium (water plus mineral particles) [34].

From Fig. 4, it can be seen that the monotonic increase in the sound speed in the bottom by 150 m s^{-1} for a depth increase of 14 m from the bottom interface must be accompanied by a monotonic increase in the density from 1.7 to 1.95 g cm^{-3} in the absence of gas in the sediments. The actual seafloor density in Fig. 4b is rather constant with depth at 1.85 g cm^{-3} than following the theoretical dependence. In our opinion, the near-surface sediment layer should be considered a three-component, i.e., containing gas whose concentration decreases with depth, leading to an increase in sound speed.

---

[2] It should be noted that random spatio-temporal fluctuations of sound speed in water, caused by ongoing hydrodynamical processes, particularly, by internal waves, can also be observed on the ocean shelf. While such fluctuations have the potential to affect the sound propagation [56] discussed in this study, they are at a significant level primarily on the Atlantic and Pacific shelves.

Figure 4. Experimental profiles of (a) sound speed and (b) sediment density at location shown by the circle in Fig. 3a. In panel b: solid line is the mean density profile over 16 drillings, gray area is confidence interval, thin wavy dashed line is profile for the deepest drilling, bold dashed line is theoretical density profile computed by panel a assuming that there is no gas in sediments.

The factors that lead to a relatively uniform distribution of gas concentration in the upper bottom sediment layer, with decreasing concentration downwards, are unknown to us. It is possible that, on the one hand, in addition to areas of active gas release, small amounts of natural gas percolate through microcracks. On the other hand, there is a mechanism that prevents gas bubbles from penetrating into the water, resulting in gas accumulation near the interface. This may be caused by the predominantly clay composition of the uppermost layer of the Holocene marine sediments. Nor can we rule out possible processes of organic matter decomposition in the near-bottom sediment layer, accompanied by gas release.

3. Acoustical model of a shallow-water waveguide with an inhomogeneous bottom

Consistent with the observational data presented in Section 2, consider a model of a waveguide composed of three layers and having a cylindrical symmetry with respect to the vertical z-axis of the cylindrical reference frame (Fig. 5). The cylindrical symmetry in the model is necessary to eliminate horizontal sound refraction when the source is placed on the symmetry axis. Here, we assume that the effects of horizontal refraction are present in reality, but that they are weak and only noticeable for tracks up to 5 km in length and for some track orientations, which will be discussed in Sections 6 and 7. We denote $r = \sqrt{x^2 + y^2}$. The water layer $0 < z < H(r)$ is assumed to have constant parameters c and ρ (the sound speed and density) and to be bounded at the top by a free space. The upper bottom layer at $H(r) < z < H_1$ is assumed to be liquid, with variable sound speed $c_1(r, z)$ and constant parameters ρ_1 and α_1. The parameters of the lower bottom layer at $H_1 < z < \infty$ match the parameters of the layer above at $z = H_1$: $c_1(r, H_1)$, ρ_1, α_1. Note that the parameters of the third layer are chosen to exclude unwanted reflections from the interface at $z = H_1$, below which there are no observational data of the seabed structure.

Let a point omnidirectional source of frequency $\omega = 2\pi f$ be located in the water layer at $0, z_0$. The sound pressure received at an arbitrary point r, z of the waveguide at time
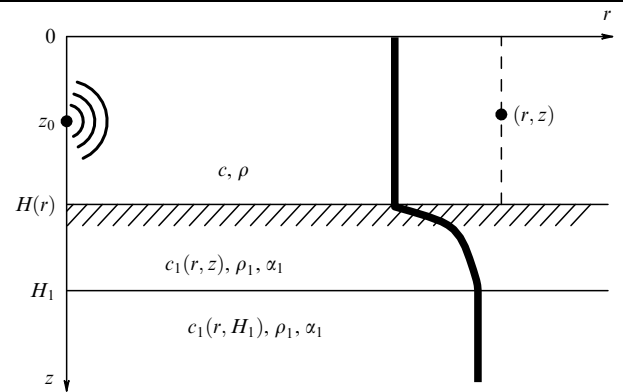
Figure 5. Model of a waveguide.

instant t will be written as $p = \mathrm{Re}\{P_A \exp(-\mathrm{i}\omega t)\}$, where $P_A = AP$ is the complex pressure amplitude, A is the quantity characterizing power and the initial phase of the source (which does not play any further role and is assumed to be $A = 1$ Pa m for certainty), and P is the Green's function found by solving the Helmholtz equation under appropriate boundary conditions [35],

$$\left\{\frac{1}{r}\frac{\partial}{\partial r}\left(r\frac{\partial}{\partial r}\right) + \frac{\partial^2}{\partial z^2} + \hat{K}^2\right\} P = -\delta(z - z_0)\frac{\delta(r)}{2\pi r},$$

$$P|_{z=0} = 0, \ P|_{z=H-} = P|_{z=H+}, \ m_1\frac{\partial P}{\partial n}\bigg|_{z=H-} = \frac{\partial P}{\partial n}\bigg|_{z=H+}, \ (3)$$

$$P|_{z=H_1-} = P|_{z=H_1+}, \ \frac{\partial P}{\partial z}\bigg|_{z=H_1-} = \frac{\partial P}{\partial z}\bigg|_{z=H_1+},$$

where

$$\hat{K} = \begin{cases} k, & 0 < z < H \\ k_1, & z > H \end{cases}, \quad k = \frac{\omega}{c},$$

$$k_1(r, z) = \frac{\omega}{c_1(r, z)}\left(1 + \mathrm{i}\frac{\alpha_1}{2}\right), \quad m_1 = \frac{\rho_1}{\rho},$$

$\delta(\cdot)$ is the Dirac delta function, and $\partial/\partial n$ is the derivative along the normal to the interface between layers. An

additional condition on (3), which emphasizes the unique solution, is the radiation condition at infinity, which in the case of an absorbing bottom is reduced to the boundedness of the field amplitude at infinity, $|P| = O(1)$ for $(r, z) \to \infty$.

A solution of problem (3) is sought in the framework of the modal approach and the method of transverse sections [2]

$$P(r, z) = \sum_{m=1}^{M} P_m(r, z) = \sum_{m=1}^{M} A_m(r; z_0)\, \psi_m(r, z)\,, \tag{4}$$

where $P_m(r, z)$ is the field of the mth mode, $A_m(r; z_0)$ is the amplitude of the mth mode, and $\psi_m(r, z)$ is the local vertical profile of the mth mode. The modal amplitudes A_m in (4) can be found in the adiabatic approximation (we will act in this way in this section) as well as taking into account mode coupling or horizontal refraction (see the following sections). The modal profiles (normalized eigenfunctions) ψ_m together with corresponding eigenvalues ξ_m are obtained from the solution to the Sturm–Liouville problem for $0 \leqslant z \leqslant H_1$:

$$\begin{cases} \psi_m'' + (\hat{K}^2 - \xi_m^2)\,\psi_m = 0\,, \quad 0 \leqslant z \leqslant H_1\,, \\[4pt] \psi_m(0) = 0\,, \\[4pt] \psi_m(H-) = \psi_m(H+)\,, \quad m_1 \psi_m'(H-) = \psi_m'(H+)\,, \\[4pt] \psi_m(H_1) + g_m \psi_m'(H_1) = 0\,, \\[4pt] \displaystyle\int_0^H \psi_m^2(z)\,\mathrm{d}z + \frac{1}{m_1}\int_H^{H_1} \psi_m^2(z)\,\mathrm{d}z + \frac{g_m}{2 m_1}\,\psi_m^2(H_1) = 1\,, \end{cases} \tag{5}$$

where for brevity we leave only the variable z on the list of arguments of the function $\psi_m(\cdot)$, and the prime denotes the derivative with respect to z. For $z \geqslant H_1$, the eigenfunctions are $\psi_m = \psi_m(H_1)\exp[\mathrm{i}\varepsilon_{1m}(z - H_1)]$. The quantities g_m and ε_{1m} will be described below. The summation in (4) is performed by the first M modes of the discrete spectrum, which are sufficient to describe the full discrete spectrum contribution in the field at the selected distance from the source. The contribution from the continuous spectrum is ignored in (4). Taking into account the estimates obtained in [35], the continuous spectrum can be ignored at distances larger than $r \sim H$ if the Pekeris branch cut is used in the modal calculations. In this case, the discrete spectrum includes, in addition to the normal modes, so-called quasi-modes, which are necessary for field calculations over a water-like bottom ($c \approx c_1$) at short distances ($r \sim (1-10)H$).

Let us explain the terms of discrete and continuous spectra, normal modes, and quasi-modes, as well as the closely related term branch cut. In any cross section of the so-called reference waveguide (i.e., a horizontally homogeneous waveguide with the parameters of the original waveguide at a distance r), a problem analogous to (3) has an exact solution, written in the integral form as $P = \int_{-\infty}^{\infty} \phi(\xi)\,\mathrm{d}\xi$. Using the residue theory, the integral can be transformed into

$$P = 2\pi\mathrm{i}\sum_{m=1}^{M} \mathrm{Res}\left[\phi(\xi),\, \xi_m\right] + \int \phi(\xi)\,\mathrm{d}\xi = \mathrm{DS} + \mathrm{CS}\,,$$

where DS is the discrete spectrum (the sum of the residues $\phi(\xi)$ at the poles $\xi_m \equiv \xi_m(r)$ for $\mathrm{Im}\,\xi \geqslant 0$) and CS is the continuous spectrum (the integral over the sides of the branch

cut beginning at the branch point $k_1(H_1) \equiv k_1(r, H_1)$, caused by the presence of the complex square root ε_{1m} in $\phi(\xi)$; see below). Note that the discrete spectrum is given by formula (4), while the continuous spectrum appears only for open waveguides, i.e., those with infinite depth.

In the transformation of the integral which is described above, the branch cut can be drawn arbitrarily. It is only important that the Jordan lemma is valid and that the residue theory is applicable. Depending on how the branch cut is drawn, the relationship between DS and CS may vary, but the net field P remains unaffected. Often, one tries to reduce the field description only to the discrete spectrum: $P \approx \mathrm{DS}$. It is therefore important to find such a branch cut that minimizes the continuous spectrum.

For the field description in the lower half-space ($z > H_1$), this is the EJP cut (after the author's names: Ewing, Jardetzky, Press), which leads to a discrete spectrum composed of a complete and finite set of normal modes [35, 53, 54]. In this case, the normal modes are particular solutions of the Helmholtz equation that satisfy the boundary condition and the radiation condition at infinity. For the field description in the upper waveguide layers ($0 < z < H_1$), in addition to the EJP cut, the Pekeris cut can be used, which gives a discrete spectrum consisting of normal modes and quasi-modes [35, 53, 54]. The quasi-modes differ from the normal modes in only one respect: they do not satisfy the radiation condition at infinity, i.e., if the quasi-modes are continued into the lower half-space, their amplitudes will grow infinitely with depth. For this reason, the Pekeris cut cannot be used in the lower half-space (the Jordan lemma is not observed). However, this property of quasi-modes does not play a negative role in their applicability region ($0 < z < H_1$), where the quasi-modes are in fact no different from the normal modes. Furthermore, the quasi-modes play a positive role, by replacing the description of the continuous spectrum from the EJP cut. Estimates [35] show that, when a few modes are excited, the use of the EJP cut leads to an approximate equality $P \approx \mathrm{DS}$ at distances larger than $r \sim 10H$ in the water layer, while the use of the Pekeris cut allows this distance to be reduced to $r \sim H$.

Note that, by using the concept of 'quasi-modes,' we follow L M Brekhovskikh [55]. In his words, the quasi-modes are "illegitimate" modes that are "quite legitimately" used in ocean acoustics, for example, in the description of soft-bottom waveguides ($c > c_1$), as well as in some adjacent branches of physics, for example, in the study of waves in electromagnetic and optical waveguides. It is worth noting that quasi-modes belong to the class of leaky modes and fully span this class in the analysis of fields in lossless waveguides.

Now, consider the solution to problem (5). It is solved in cross sections for each fixed r. Taking into account the homogeneity of the water layer and the lower bottom layer, we find from (5)

$$\psi_m = N_m \begin{cases} \sin(\varepsilon_m z)\,, & 0 \leqslant z \leqslant H\,, \\[4pt] \bar{\psi}_m(z)\,, & H \leqslant z \leqslant H_1\,, \\[4pt] \bar{\psi}_m(H_1)\exp\left[\mathrm{i}\varepsilon_{1m}(z - H_1)\right]\,, & z \geqslant H_1\,, \end{cases} \tag{6}$$

$$\varepsilon_{1m} = \begin{cases} \varepsilon_{1m}^M\,, & \xi_m \notin C\,, \\[4pt] -\varepsilon_{1m}^M\,, & \xi_m \in C\,, \end{cases} \tag{7}$$
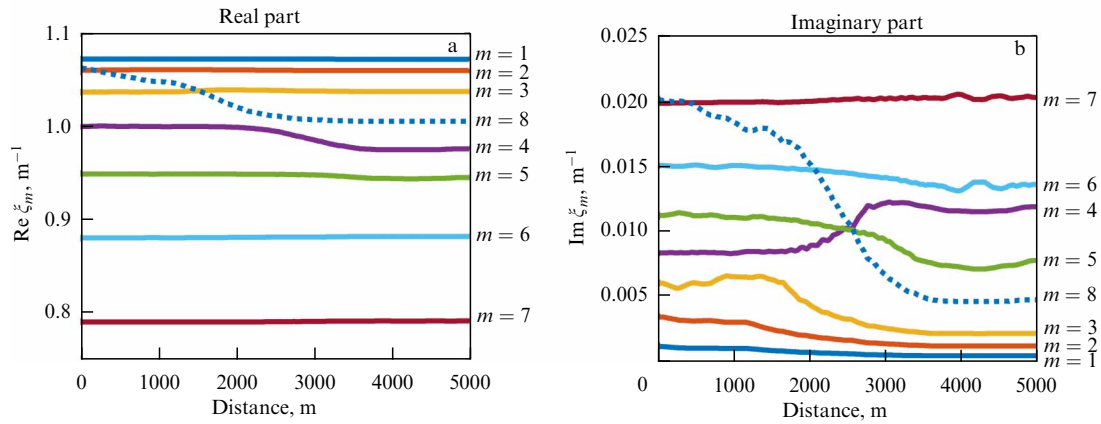
Figure 6. (a) Real and (b) imaginary parts of eigenvalues of waveguide modes as functions of distance along path 4 from left to right.

where $\bar{\psi}_m(z)$ is the solution to the Sturm–Liouville problem for $H \leqslant z \leqslant H_1$,

$$
\begin{cases}
\bar{\psi}_m'' + (k_1^2 - \xi_m^2)\,\bar{\psi}_m = 0, & H \leqslant z \leqslant H_1\,, \\
\bar{\psi}_m(H) = \sin(\varepsilon_m H), & \bar{\psi}_m'(H) = m_1 \varepsilon_m \cos(\varepsilon_m H), \\
\bar{\psi}_m(H_1) + g_m \bar{\psi}_m'(H_1) = 0,
\end{cases}
\tag{8}
$$

$$
N_m = \left(\frac{H}{2} - \frac{\sin(2\varepsilon_m H)}{4\varepsilon_m} + \frac{1}{m_1}\int_H^{H_1} \bar{\psi}_m^2(z)\,\mathrm{d}z + \frac{g_m}{2m_1}\bar{\psi}_m^2(H_1) \right)^{-1/2},
$$

$\varepsilon_m = \sqrt{k^2 - \xi_m^2}$, $\varepsilon_{1m}^M = \sqrt{k_1^2(H_1) - \xi_m^2}$, $g_m = \mathrm{i}/\varepsilon_{1m}$, and C is the domain in which the conditions $\mathrm{Im}\,\varepsilon_{1m}^M < 0$ and $\mathrm{Re}\,\xi_m > \mathrm{Re}\,k_1(H_1)$ hold.

All square roots $\sqrt{\cdot}$ in the above formulas and further in the text are understood in the same way as the principal value[3] of a complex square root, such that $\mathrm{Re}\,\sqrt{\cdot} > 0$. If $\mathrm{Re}\,\sqrt{\cdot} = 0$, then the value with $\mathrm{Im}\,\sqrt{\cdot} > 0$ is taken. We note that such a rule for root selection is implemented in the Matlab software (the sqrt function).

Formula (7) for computing the square root on the upper sheet of a Riemann surface of a complex plane ξ, where the eigenvalues ξ_m of the Sturm–Liouville problem (8) are sought, corresponds to the choice of the Pekeris cut, which is drawn vertically upwards from the branch point $k_1(H_1)$. As mentioned above, for open waveguides lying on a liquid half-space, the Pekeris cut minimizes the contribution of the continuous spectrum in the full field in the region above the boundary of the half-space, i.e., in water and in the bottom to depth H_1, as compared to the EJP cut. This is explained by the presence in the discrete spectrum of not only normal modes ($\mathrm{Im}\,\varepsilon_{1m} > 0$) but also quasi-modes ($\mathrm{Im}\,\varepsilon_{1m} < 0$) in the case of the Pekeris cut.

We mention the peculiarities of the numerical solution of the Sturm–Liouville problem (8). As is well known, the solution to this problem is reduced to finding the roots ξ_m of an equation of the form $\Phi(\xi) = 0$, which is the boundary condition at the lower boundary. A technique for finding ξ_m directly was proposed. First, in a prescribed rectangular search domain in the complex ξ-plane, on a sufficiently dense nonuniform grid, local minima of the function $|\Phi(\xi)|$ were determined. Then, the position of the local minima, i.e.,

the position of ξ_m, was refined by recursive subdivision until the required accuracy was achieved. It was found that, when moving from one transverse section to another in the case of inhomogeneous tracks, the positions of ξ_m on the complex plane also change continuously (see Fig. 6, which shows the real and imaginary parts of ξ_m at a frequency of 250 Hz as a function of the coordinate along track 4 marked in Fig. 3a). In some cross sections, unusual situations were observed where the complex eigenvalue of one mode appeared directly above the analogous value for another mode, $\mathrm{Re}\,\xi_m = \mathrm{Re}\,\xi_n$, $\mathrm{Im}\,\xi_m \neq \mathrm{Im}\,\xi_n$ (see the behavior of the dashed line in Fig. 6). We note that, in such situations, and also for a sufficiently high coefficient of sound attenuation in the bottom, characteristic of the Arctic shelf, the use of standard computational software (such as KRAKEN) to find ξ_m can lead to errors. The technique of finding the eigenvalues ξ_m and also the eigenfunctions ξ_m in a waveguide which is inhomogeneous along the track is presented in more detail in Refs [27, 41].

Note that, for a homogeneous bottom model with $k_1 = \mathrm{const}$, (4)–(7) lead to well-known expressions for $\psi_m(z)$ for the Pekeris waveguide [1, 37].

Based on (4), for $r \geqslant r_0$, the intensity $I(r, z) = (2\rho c)^{-1}|P_A|^2$, the depth average intensity $\bar{I}(r) = H^{-1}\int_0^H I(r, z)\,\mathrm{d}z$, and the logarithmic intensity (attenuation curve)

$$
J(r) = 10\lg \frac{\bar{I}(r)}{\bar{I}(r_0)} + 10\lg \frac{r}{r_0}
\tag{9}
$$

are calculated. We will take the values of r and r_0 such that the field is well described by the discrete spectrum of modes only, while the contribution from the continuous spectrum is small. Note that formula (9) differs from formula (1) in that it is written for the depth averaged sound field intensity. This averaging, as well as averaging over the distance r in the interval exceeding the period of interference beats, serves to eliminate the variations in intensity caused by intermodal interference.

We also note that $\bar{I}(r)$ depends on the source depth z_0; however, this dependence is weak provided the source is located further than one wavelength from the waveguide boundaries [36]. We will use this in the calculations below.

The quantity $J(r)$ is related to the value of transmission loss [38] $TL = 10\lg[\bar{I}(r = 1\ \mathrm{m})/\bar{I}(r)]$, which is accepted in hydroacoustics, by the following relationship:

$$
J(r) = 10\lg \frac{\bar{I}(r = 1\ \mathrm{m})}{\bar{I}(r_0)} + 10\lg \frac{r}{r_0} - TL\,.
\tag{10}
$$

---

[3] The second, not principal, value of the complex square root differs from the principal one by its sign.

The curves $J(r)$, calculated for different tracks and sound frequencies, will be considered the main result of the numerical experiment; they can be obtained in observations by recording signals with the help of a vertical hydrophone array crossing the entire water column.

4. Sound propagation in a waveguide with smooth inhomogeneities

Assuming that the water–bottom interface is horizontally smooth, which implies $\partial/\partial n \approx \partial/\partial z$, solution (4) in the adiabatic approximation (without considering mode coupling and refraction) takes the form [35]

$$P(r,z) = \frac{\exp(i\pi/4)}{\sqrt{8\pi}} \sum_{m=1}^{M} \frac{\psi_m(0,z_0)}{\sqrt{rq_m(r)}} \exp\left(i\int_0^r \xi_m(r')\,dr'\right)\psi_m(r,z),$$ (11)

where $q_m = \mathrm{Re}\,\xi_m$. In this case, the complex modal amplitudes are written as

$$A_m(r;z_0) = \frac{\exp(i\pi/4)}{\sqrt{8\pi}} \frac{\psi_m(0,z_0)}{\sqrt{rq_m(r)}} \exp\left(i\int_0^r \xi_m(r')\,dr'\right).$$

4.1 Dependence of transmission loss on the sound speed in the bottom

In order to explain the aspects of sound propagation in a waveguide with an inhomogeneous bottom, we start with a limit case where the bottom is a homogeneous half-space with constant parameters. The sound speed in the bottom will vary in wide limits $c_1 = 100-1700$ m s^{-1}: from an acoustically soft bottom ($c_1 < c$) to an acoustically hard bottom ($c_1 > c$). The other parameters are taken as follows:

$c = 1467$ m s^{-1} is the sound speed in water, $\rho = 1$ g cm^{-3} is the water density, $\rho_1 = 1.6$ g cm^{-3} is the seabed density, $\alpha_1 = 0.02$ describes the loss in the bottom, and $H = 120$ m is the waveguide depth. It should be noted that a shallow hydroacoustical waveguide with a practically constant sound speed in water is characteristic, e.g., of the Barents Sea in spring.

To estimate the sound attenuation with distance, we calculate the intensity of the sound field averaged over all depths of the source z_0 and the receiver z in the range from 0 to H,

$$\bar{\bar{I}}(r) = \frac{1}{H^2}\int_0^H \int_0^H \frac{\left|P_A(r,z,z_0)\right|^2}{2\rho c}\,dz\,dz_0.$$ (12)

We insert the resulting dependence $\bar{\bar{I}}(r)$ into (9) in place of $\bar{I}(r)$. As shown by simulations, the dependences $\bar{\bar{I}}(r)$ and $\bar{I}(r)$ practically coincide when the source is separated from boundaries by a wavelength or more. For this reason, replacing $\bar{I}(r)$ with $\bar{\bar{I}}(r)$ is appropriate. The distance r_0 in (9) for which the continuous spectrum can be ignored is in this example $r_0 = 300$ m. The results of simulations for different speeds of sound in the bottom and for sound frequencies of 50 and 300 Hz are shown in Fig. 7 [39].

As can be seen from Fig. 7, there is strong sound attenuation for a soft bottom; it is most pronounced at low frequencies and when the sound speed c_1 is close to the sound speed in the water layer ($c_1 \approx c$, a water-like bottom). In this case, the waveguide propagation is only related to the difference in density between water and the bottom. For a water-like bottom, the intensity drops by 30 dB compared to a hard bottom ($c_1 = 1700$ m s^{-1}) or very soft bottom ($c_1 = 100$ m s^{-1}) already at the distance $r = 5$ km from the source. It should be emphasized that the
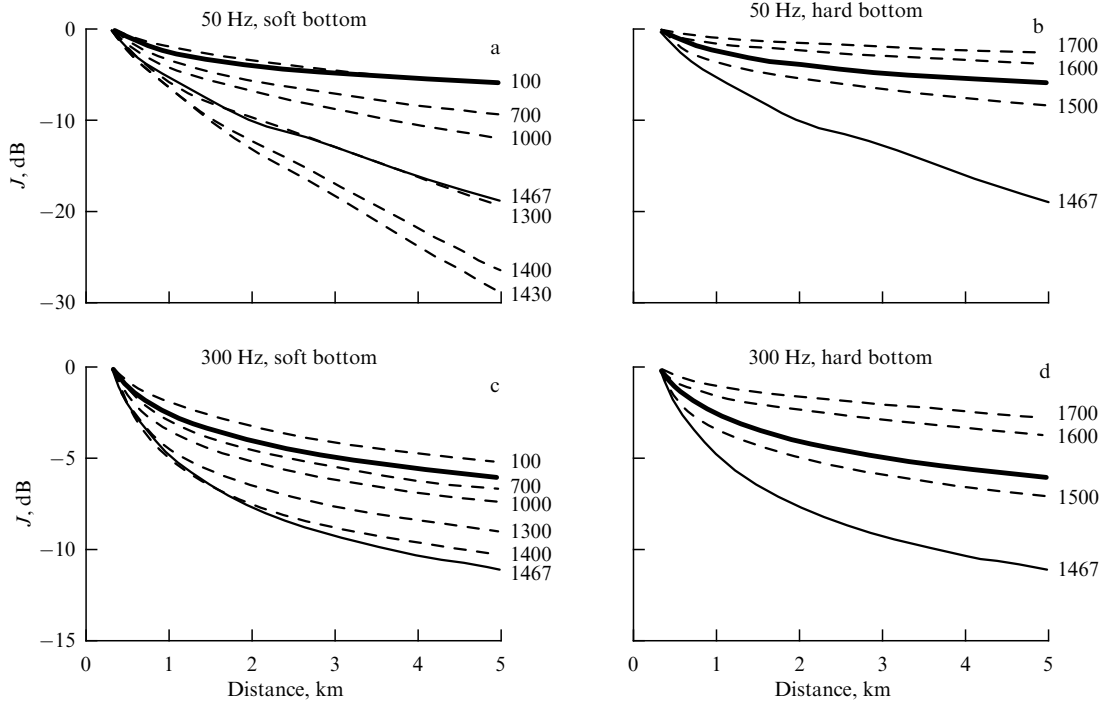
Figure 7. Decay of mean intensity in dB for (a, c) a soft and (b, d) a hard bottom for a constant sound speed in the water layer. Magnitude of c_1 (m s^{-1}) in the bottom is indicated near the curves. Solid thin line corresponds to equal sound speeds in water and the bottom (1467 m s^{-1}). Bold line is the dependence (13) — the '3/2 law.' Panels (a) and (b) correspond to a sound frequency of 50 Hz, and (c) and (d) correspond to 300 Hz.
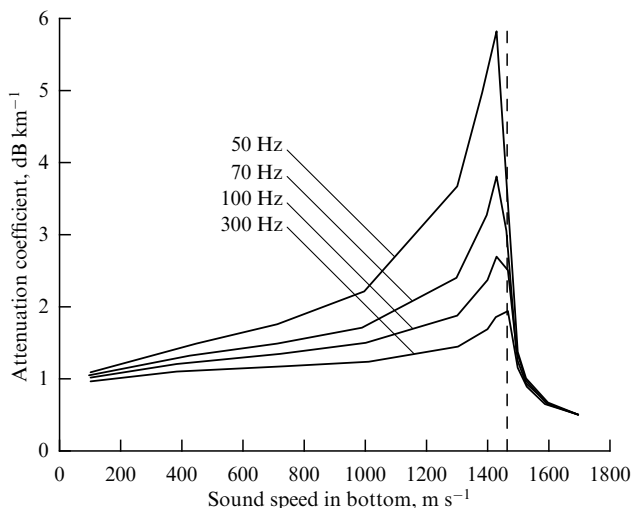
Figure 8. Dependence of attenuation coefficient β on the sound speed in the bottom for constant sound speed in the water layer. Sound frequency is given in the figure. Vertical dashed line marks sound speed in water.

anomalously high attenuation due to absorption in the bottom ($\alpha_1 \neq 0$) occurs when the values of c_1 differ slightly from the values of c. For $\alpha_1 = 0$, anomalously high attenuation is observed for $c_1 = c$.

The dependence of sound attenuation on c_1 can be graphically illustrated using a technique accepted in engineering hydroacoustics by approximating each line shown in Fig. 7 by a straight line, using the slope of this line to estimate the mean intensity decay rate for different frequencies. The slope coefficient β is called the attenuation coefficient. Figure 8 shows the resulting dependences of β as a function of the sound speed in the bottom at fixed values of frequencies of 50, 70, 100, and 300 Hz. For a soft bottom, the value of β increases monotonically as the sound speed in the bottom increases, and for a hard bottom, it decreases monotonically. The maximum of β is reached, as expected, when the sound speeds in water and the bottom are approximately equal. If c differs significantly from c_1, regardless to which side, the reflection from the bottom is additionally increased due to the interfacial jump in the sound speeds, and the attenuation decreases. The maximum of β for a soft bottom is highly frequency dependent. If the frequency is reduced from 300 to 50 Hz, the maximum of β increases from approximately 2 to 6 dB km^{-1} (for $\alpha_1 = 0$ up to 10 dB km^{-1}). This is mainly related to the fact that, for a waveguide mode with the same number, the attenuation coefficient decreases with increasing frequency.

It is interesting to compare these numerical results with the well-known simplified analytical dependence for shallow basins with a constant sound speed — the so-called '3/2 law' [1]:

$$I_{3/2}(r) \approx \frac{I(r_0)}{r_0^{-3/2}} \, r^{-3/2} . \tag{13}$$

From Fig. 7, it can be seen that the approximate law (13) describes the waveguides with a hard bottom better. For a soft bottom, dependence (13) gives values that are too high, which is explained by the presence of only leaky modes in the soft bottom case, leading to a higher energy removal from the waveguide.

It is interesting to note that, for low frequencies and almost equal speeds of sound in the bottom and in water, not only does the intensity decrease with distance much more than predicted by formula (13), but it also decreases more than in a free space, where $I_{\text{sph}}(r) = I(r_0)(r/r_0)^{-2}$. This is due to the fact that in this case we are dealing with sound radiation in the vicinity (at distances comparable to the wavelength) of the reflecting upper boundary, which is known to have a dipole character [1]. It should be remembered that, for dipole radiation, $I_{\text{dip}}(r) = I(r_0)(r/r_0)^{-4}$.

4.2 Sound attenuation in a waveguide with an inhomogeneous bottom

In order to analyze the transmission loss for a bottom model based on seismic survey data (see Section 2), we consider four tracks, each 5 km in length. They are shown in Fig. 3a by lines numbered 1–4. Tracks 1–3 are located in regions with an approximately homogeneous bottom structure, which differs among the tracks. Track 1 has a water-like bottom. In terms of the color scale in Fig. 3a, tracks 1, 2, and 3 lie in dark, light, and intermediate regions. Track 4 is essentially nonuniform, with one half lying over a dark region and the other half over a light region. Figure 9 shows vertical transects of the sound speed field in the bottom for tracks 1–4.

The thickness of the water layer is $H = 28$ m for tracks 1, 2, and 4, and $H = 32$ m for track 3. The water–bottom interface is represented by a dashed line in Fig. 9. The sound speed in water is $c = 1460$ m s^{-1}.

The sound speed in the bottom $c_1(r, z)$ was taken from experimental data for each track (Fig. 9). The bottom density was equal to $\rho_1 = 1.85$ g cm^{-3}, and the loss in the bottom were given by the parameter β_{1f} mentioned above. Note that the available observational data on the sound speed profile were limited to a depth of 80 m.

The source frequencies of 137 and 250 Hz are taken the same as in Ref. [36]. It will be noted that these frequencies correspond to local maxima in the low-frequency part of the spectra of signals emitted by whales on the Arctic shelf. (We mean the protected species of whales found in the Arctic.) The sound source was placed approximately in the center of the water layer at a depth of $z_0 = 15$ m.

For all four tracks (Fig. 3a, 9), the source is located at the leftmost point of the track and is fixed, while a distributed receiver measuring the depth-averaged intensity is moved from the source to the right, so that the source–receiver distance varies in the range $r_0 \leqslant r \leqslant 5$ km, where $r_0 = 100$ m. From a distance of 100 m, the field is well described by the discrete spectrum of modes, and the contribution of the continuous spectrum is small. For track 4, we also consider an inverse case, where the source is at the rightmost point, and the receiver is moved to the left. Note that, in practice, the role of the distributed receiver, measuring the depth-averaged intensity, can be played by a vertical array of hydrophones placed half a wavelength apart.

Figure 10a–d shows the attenuation curves $J(r)$ simulated in the adiabatic approximation (i.e., the sums of independent modes) according to (9) for tracks 1–4 and frequencies of 137 and 250 Hz, obtained by moving the receiver to the right of the source fixed at the leftmost positions on the tracks. The ratio of the distance to the water column thickness varies for tracks 1, 2, and 4 in the limits $r/H = 3.6 - 179$, and for track 3 it is $r/H = 3.1 - 156$.
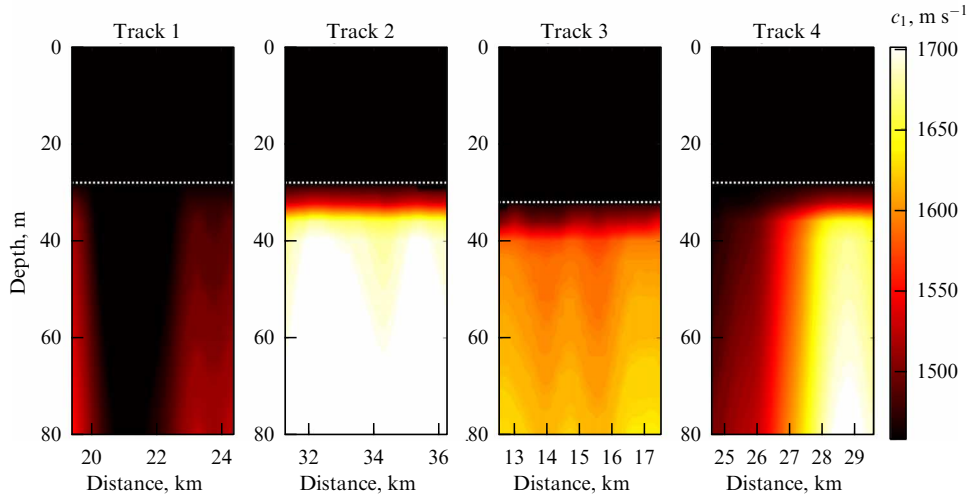
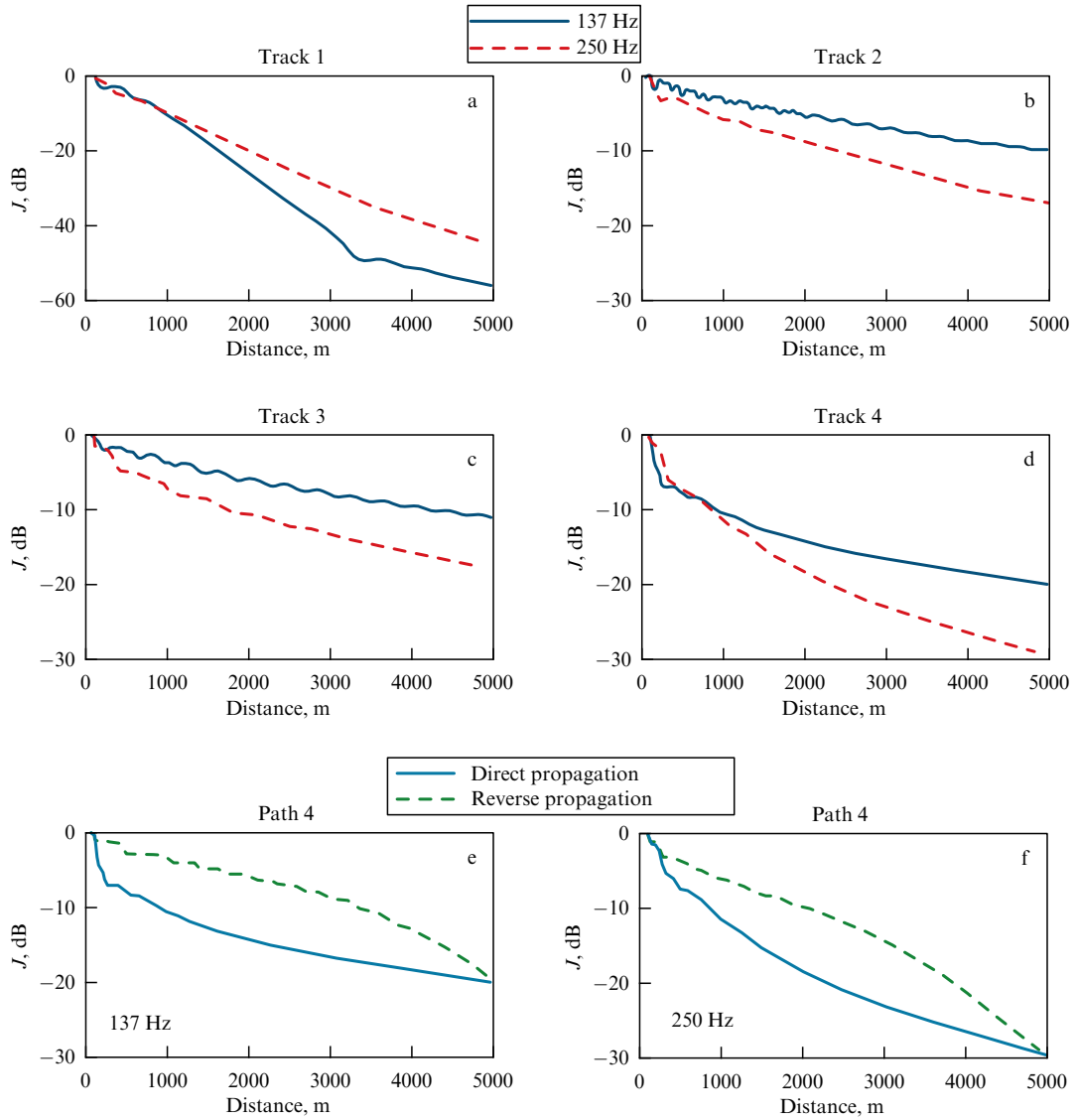**Figure 9.** Vertical profiles of sound speed for acoustical tracks 1–4 shown in Fig. 3a.

Figure 10. Attenuation curves in adiabatic approximation for acoustical tracks 1–4 (a–d) for frequencies of 137 Hz (solid line) and 250 Hz (dashed line). Analogous curves for track 4 and propagation in direct and inverse directions are shown in d, e.

Figure 10e, f shows for comparison the case of track 4 with the source placed not only in the leftmost position but also in the rightmost position (the receiver is moved to the left). In the latter (inverse) case, the attenuation curve will be denoted $J_{\text{inv}}(r)$.

Let us summarize the main details of sound decay that follow from Fig. 10.

(1) For a fixed sound frequency, the decay increases (the attenuation curves shift downwards) as the mean sound speed in the bottom $\bar{c}_1$ (for $\bar{c}_1 > c$) decreases. This is explained by the decrease in the reflection coefficient for a weaker contrast between the media. For $\bar{c}_1 \approx c$ (track 1, water-like bottom), the sound attenuation is anomalously high (up to 20 dB km^{-1}), which is probably a characteristic feature of certain regions of the Arctic shelf. Note that, in the case of a soft bottom, when $\bar{c}_1$ is significantly smaller than c (by more than 100 m s^{-1}), the attenuation curves behave in the opposite way (see Fig. 7). Such behavior was found by the authors in shallow freshwater regions [39].

(2) For a higher sound frequency, the attenuation curves generally shift downwards (higher loss), which is explained by the frequency dependence of β_{1f} (tracks 2–4), except for the case when $\bar{c}_1 \approx c$ (track 1). Additional simulations for other values of β_{1f} showed that, regardless of the model function $\beta_{1f}(f)$ chosen by us, there is an anomalously high attenuation of sound for $\bar{c}_1 \approx c$. In this case, all or almost all modes turn out to be leaky and carry energy away from the water layer. We note that an increase in sound attenuation in the water layer with frequency was observed in studies conducted by the GPI RAS in the Barents Sea.

(3) For $r > 1$ km, the functions $J(r)$ transform into straight lines, and for $r < 1$ km, there is an irregular interval where the shape of the curves has a slightly wavy character. The slope of the curves varies from 1.5 to 20 dB km^{-1} for a frequency of 137 Hz and from 2 to 10 dB km^{-1} for a frequency of 250 Hz. Comparing Fig. 10b–d, it can be seen that the attenuation curves $r > 1$ are similar except for Fig. 10a and the frequency of 137 Hz, and also Fig. 10e, f for the inverse propagation, where a significant change in the slope angle of the curves is observed.

(4) The curves in Fig. 10e, f show an approximate equality of attenuation at a distance of 5 km for direct (from left to right) and inverse (from right to left) sound propagation, i.e., when the source and receiver are exchanged. This fact is a consequence of the reciprocity theorem (or principle), according to which the sound field is invariant with respect to the exchange of point source and receiver [40]. The approximate nature of our result is due to the use of a distributed receiver in the form of a vertical array intersecting the entire water column. For other distances other than 100 m and 5 km, the curves of $J(r)$ and $J_{\text{inv}}(r)$ diverge significantly, by almost 10 dB. This is caused by a significant change in the vertically mean sound speed in the bottom along track 4 (see Fig. 9). As a result, the depth of sound penetration in the bottom, and hence the attenuation, is different at different intervals of the track.

Next, we turn to the question of selecting c_1^{eff} — the effective sound speed in the bottom — based on the attenuation curves (see Section 1). In Ref. [27], it is shown that, due to the difference between $J(r)$ and $J_{\text{inv}}(r)$ on highly inhomogeneous tracks, the value of c_1^{eff} should be chosen by minimizing the differences in attenuation at the end point of the track, and not for the whole track. We mean the differences among

the attenuation curves[4] shown in Fig. 10 and similar curves calculated for the model of a bottom as a homogeneous half-space with the sound speed c_1^{eff}. Reference [27] also shows that the mean sound speed in the bottom defined as a double integral over the distance r and depth h,

$$\bar{c}_1(r,h) = \frac{1}{rh} \int_0^r \int_H^{H+h} c_1(r',z) \, \mathrm{d}z \, \mathrm{d}r', \tag{14}$$

is approximately the value of c_1^{eff} for $h \approx 0.6\lambda_1$, where $\lambda_1 = c_1^{\text{eff}}/f$. In other words, the effective sound speed in the bottom is approximately the real sound speed in the bottom averaged over the track and over the depth equal to $0.6\lambda_1$.

5. Accounting for mode coupling in describing a sound field

We abandon the adiabatic approximation and continue by treating the sound field further as the sum of coupling modes. A solution to problem (3) that satisfies the appropriate boundary conditions and the radiation condition at infinity, taking into account mode coupling, is written as [37]

$$P(r,z) = \sum_{m=1}^M C_m(r) \frac{\psi_m(r,z)}{\sqrt{q_m(r)\, r}} \exp\left(\mathrm{i} \int_0^r q_m(r') \, \mathrm{d}r' \right), \tag{15}$$

where $C_m(r)$ are the modal excitation coefficients given for $r = 0$ by the formula $C_m(0) = [\exp(\mathrm{i}\pi/4)/\sqrt{8\pi}]\, \psi_m(0,z_0)$. (Note that, in solution (15), as before, the term due to the continuous spectrum is omitted because of its smallness.)

In order to obtain the coefficients $C_m(r)$ for $r > 0$, we insert (15) into (3), with zero on the right-hand side of the Helmholtz equation. Using standard approximations which disregard all terms in higher orders of smallness (as done in [37]), and also using the equation for the eigenfunctions $\psi_m'' + (\hat{K}^2 - \xi_m^2)\, \psi_m = 0$, we find

$$\sum_{n=1}^M (\psi_n E_n)\, C_n' = -\sum_{n=1}^M C_n \left(\frac{\partial \psi_n}{\partial r} + \frac{\gamma_n}{2}\, \psi_n \right) E_n, \tag{16}$$

where for convenience of further presentation we replaced the summation index $m \to n$, $C_n' = (\mathrm{d}C_n)/\mathrm{d}r$, $E_n = \sqrt{q_n} \exp(\mathrm{i} \int_0^r q_n(r')\, \mathrm{d}r')$, and $\gamma_n/2 = \operatorname{Im} \xi_n$.

Furthermore, we will need the orthogonality condition for the eigenfunctions in the form [37]

$$\int_0^{H_1} \frac{\rho}{\rho(z)} \psi_m \psi_n \, \mathrm{d}z + I_{mn} = \delta_{mn}, \tag{17}$$

where

$$\rho(z) = \begin{cases} \rho, & 0 \leqslant z \leqslant H \\ \rho_1, & z > H \end{cases}, \quad I_{mn} = \frac{\mathrm{i}\psi_m(H_1)\,\psi_n(H_1)}{m_1(\varepsilon_{1m} + \varepsilon_{1n})}.$$
$$\delta_{mn} = \begin{cases} 1, & m = n \\ 0, & m \neq n \end{cases}.$$

The parameter $\varepsilon_{1m,n}$ is calculated according to (7). It is important that we use the Pekeris cut as before and consider both the normal modes and the quasi-modes. We mention that the orthogonality condition in the form of

---

[4] Recall that the attenuation curves shown in Fig. 10 can be measured experimentally.

(17) and also the related normalization rule for the eigenfunctions for $m = n$ are the same for the normal modes and the quasi-modes.

We use (17) to exclude the depth dependence of the eigenfunctions from (16). To do this, we multiply both sides of (16) by $\psi_m \rho / \rho(z)$ and integrate over the depth from 0 to H_1. Repeating this operation for the indices $m = 1, \dots, M$, we obtain the system of M linear equations

$$\sum_{n=1}^{M} \left[(\delta_{mn} - I_{mn}) E_n \right] C_n' = - \sum_{n=1}^{M} C_n \left[V_{mn} + \frac{\gamma_n}{2} (\delta_{mn} - I_{mn}) \right] E_n ,$$

(18)

$$V_{mn} = \int_0^{H_1} \frac{\rho}{\rho(z)} \psi_m \frac{\partial \psi_n}{\partial r} \, dz ,$$

(19)

where V_{mn} are the mode coupling coefficients.

Solving system (18) for known $C_m(r)$ gives the values of the derivatives $C_m'(r)$, which allows the modal coefficients to be calculated at the next step $C_m(r + \Delta r) = C_m(r) + C_m'(r)\Delta r$. As a consequence, knowing $C_m(0)$, the functions $C_m(r)$ can be found for any r.

We emphasize that the procedure described for determining $C_m(r)$ from the solution of system (18) takes into account the interaction of all modes, both normal and quasi-modes. This can be important for waveguides in which $c_1 < c$ or $c_1 \approx c$, where all or almost all modes are leaky, and where the contribution of quasi-modes, which belong to the class of leaky modes, can be significant. We also note that condition (17) differs from its known analog, which only considers the interaction of normal modes [37]. In the known approach, the normal modes form a discrete spectrum when the EJP cut is used [35]. In the lower half-space for $z \geqslant H_1$, the normal mode eigenfunctions $\psi_m = \psi_m(H_1) \exp \left[i\varepsilon_{1m}(z - H_1) \right]$ decay with depth, since for them $\text{Im} \, \varepsilon_{1m} > 0$. In this case, we have

$$I_{mn} = \frac{i\psi_m(H_1)\psi_n(H_1)}{m_1(\varepsilon_{1m} + \varepsilon_{1n})} = \int_{H_1}^{\infty} \frac{\rho}{\rho(z)} \psi_m \psi_n \, dz ,$$

and condition (17) takes the form

$$\int_0^{\infty} \frac{\rho}{\rho(z)} \psi_m \psi_n \, dz = \delta_{mn} .$$

(20)

Using (20) leads to a system analogous to (18),

$$\sum_{n=1}^{M} (\delta_{mn} E_n) C_n' = - \sum_{n=1}^{M} C_n \left(U_{mn} + \frac{\gamma_n}{2} \delta_{mn} \right) E_n ,$$

(21)

$$U_{mn} = \int_0^{\infty} \frac{\rho}{\rho(z)} \psi_m \frac{\partial \psi_n}{\partial r} \, dz ,$$

(22)

which, thanks to the Kroneker symbol δ_{mn}, is solvable in terms of derivatives, taking the classical form[5] [2]

$$C_m' = - \frac{\gamma_m}{2} C_m - \sum_{n=1}^{M} U_{mn} \frac{E_n}{E_m} C_n .$$

Its approximate solution[6] can be written in the following form:

$$C_m(r) = C_m(0) \exp \left[\left(- \frac{\gamma_m}{2} - U_{mm} \right) r \right]$$

$$+ \, i \sum_{n=1, n \neq m}^{M} \sqrt{\frac{q_n}{q_m}} \, C_n(r) \frac{U_{mn}}{\Delta q_{nm}(r)} \left[\exp \left(i\Delta q_{nm} r \right) - 1 \right] , \quad (23)$$

where $\Delta q_{nm} = q_n - q_m$.

The absence of mode coupling implies the smallness of the parameter

$$\tilde{\kappa} \approx \frac{|U_{mn}|}{|\Delta q_{nm}|} \ll 1 .$$

(24)

Inequality (24) can be rewritten in a different form if we consider that $1/|\Delta q_{nm}|$ is a quantity of the order of the length of the ray cycle in channel D, and $|U_{mn}| \approx \tilde{L}_k^{-1}$, where $\tilde{L}_k$ is the characteristic scale on which the waveguide properties (e.g., the bottom properties) vary. Inequality (24) takes the form

$$\tilde{\kappa} \approx \frac{D}{\tilde{L}_k} \ll 1 .$$

(25)

The parameter $\tilde{\kappa}$ can be called the degree of waveguide nonadiabaticity.

If the coefficients V_{mn} and U_{mn} are equal to zero, it can be shown that we return to the approximation of noninteracting modes [41], and formula (15) transforms into formula (11). Under the condition of adiabatic approximation, each mode propagates independently of other modes. In the presence of interactions, sound propagation in the waveguide is accompanied by an energy exchange between the modes, the magnitude of which is defined by the absolute value $|V_{mn}|$.

Note that the amounts of energy scattered from one mode into the other and vice versa, described by the coefficients V_{mn} (expression (19)), are not equal, i.e., $|V_{mn}| \neq |V_{nm}|$. Indeed, we differentiate (17) over the variable r for $m \neq n$. We find $V_{mn} + V_{nm} + dI_{mn}/dr = 0$, which implies $|V_{mn}| \neq |V_{nm}|$. For the coefficients U_{mn}, a similar differentiation gives $|U_{mn}| = |U_{nm}|$.

The results of numerical simulations of sound propagation in a shallow-water waveguide, taking into account mode coupling, are given further in Sections 5.1 and 5.2. (For details see [41].)

5.1 Details of mode coupling as a function of the sound speed in the bottom

In order to develop a general understanding of mode coupling caused by bottom inhomogeneities, we calculate $|V_{mn}|$ for an idealized model of the bottom, where we set the thickness of the bottom layer at $H < z < H_1$ to zero. In other words, we assume that c_1 does not depend on z, but only on r, and that the dependence is linear, $c_1 = c_0 + c_1' r$, where $c_0 = 100 \text{ m s}^{-1}$, $c_1' = 0.23 \text{ s}^{-1}$. These values imply that, for $r = 0 \dots 10$ km, the sound speed in the bottom varies in the range $c_1 = 100 \dots 2400 \text{ m s}^{-1}$. The other waveguide parameters

---

[5] There is a typo in [37]: there should be no imaginary unit before the sum symbol in formula (3.143).

[6] It is assumed that $q_m(r)$, $\gamma_m(r)$, and $\psi_m(r)$ are weakly varying functions and that the combination $\sqrt{q_n/q_m} \, C_n(r) U_{mn}$ varies slowly compared to $\exp \left(i\Delta q_{nm} r \right)$.
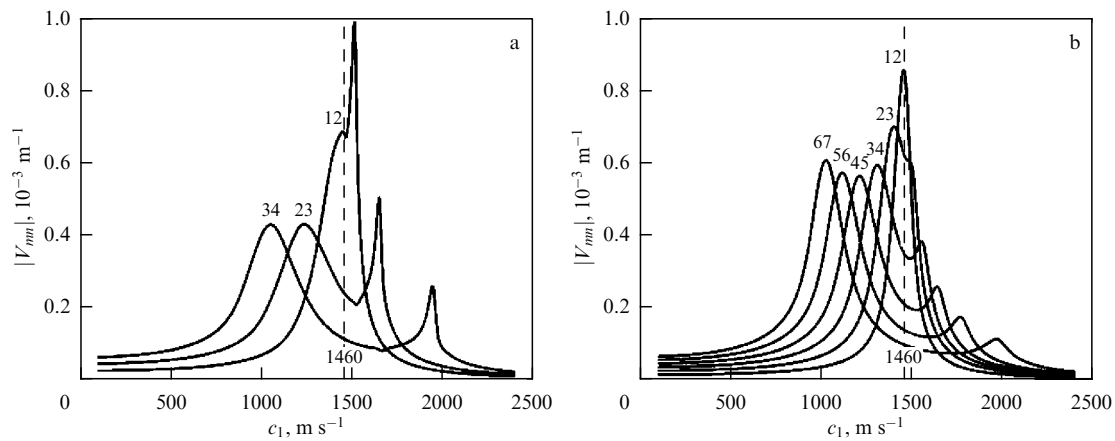
Figure 11. Absolute values of coupling coefficients for neighbor mode pairs in the idealized model of an inhomogeneous bottom. Mode numbers mn are given near the respective curves. (a) $f = 137$ Hz, (b) $f = 250$ Hz.

are taken as in Section 4.2 for $H = 28$ m. Taking into account a one to one relation between c_1 and r, we consider the dependences $|V_{mn}(c_1)|$ for the pairs of neighboring modes which interact most strongly (Fig. 11).

From Fig. 11, it can be seen that such dependences are not monotonic. Each curve has two local maxima, except curves 12 and 23 for a frequency of 250 Hz, where two maxima merge in one. The left peak is located on the side of the soft bottom ($c_1 < c$), the right one corresponds to the hard bottom ($c_1 > c$), and either can be dominant. The distance from the peak positions to the sound speed in water ($c = 1460$ m s^{-1}) increases with the number of coupling modes. The highest peak, corresponding to maximal coupling, is observed for mode pair 12 for $c_1 \approx c$ (a water-like bottom). We note that the maximum value of the coupling coefficient, $\sim 10^{-3}$ m^{-1}, obtained for sound speed inhomogeneities in the bottom, corresponds, for example, to the coefficient of interaction between the 1st and 2nd modes in a waveguide with the same depth and sound speed, but with an absolutely rigid sloping bottom. The slope angle in this case should be $1.7°$.

The maxima for a soft bottom are explained by the fact that, first, as c_1 decreases from the value c, the energy of the modes in the bottom is increased due to the increase in the amplitude and deeper penetration into the bottom. It can be said that in this case each mode becomes increasingly leaky, leading to an increase in the energy scattered between the modes due to irregularities in the bottom, which is equivalent to an increase in $|V_{mn}|$. Conversely, as c_1 continues to decrease, the energy of the modes in the bottom decreases due to the increase in the reflection coefficient at the water–bottom interface. This leads to a reduction in $|V_{mn}|$, even though the modes remain leaky. As a result, there is an optimum c_1 for each mode pair where $|V_{mn}|$ reaches a maximum, i.e., where the mode coupling is maximal in the soft bottom range.

For a hard bottom, the maxima of the mode coupling are related to the moment when the propagating modes turn into leaky modes, i.e., when the condition $\mathrm{Re}\,\xi_m = \mathrm{Re}\,k_1$ holds. In the ray treatment, when this condition is fulfilled, the Brillouin rays corresponding to the modes pass through the critical angle for the water–bottom interface. For example, at a frequency of 137 Hz, this happens for modes 2, 3, 4 when $c_1 = 1528, 1665, 1965$ m s^{-1}, respec-

tively, which practically coincides with the right peaks on curves 12, 23, 34 (Fig. 11a). The physical situation is such that, when the Brillouin rays corresponding to mode 3, for example, pass through the critical angle (this happens for $c_1 = 1665$ m s^{-1}), a strong scattering of these rays (of this mode) is observed into all other rays (modes) and also into the continuous spectrum. For this reason, in Fig. 11a, a maximum of the quantity $|V_{23}|$ is observed at $c_1 \approx 1665$ m s^{-1}, which characterizes the energy scattered from mode 3 into mode 2. In general, all curves like $|V_{m3}|$, as follows from the calculations, reach the right maximum for the same value $c_1 \approx 1665$ m s^{-1}, which corresponds to the scattering of mode 3 into mode m when passing through the critical angle. However, the curve $|V_{32}|$, which characterizes the energy scattered from mode 2 into mode 3, has the right maximum for the other value $c_1 \approx 1528$ m s^{-1}, as do all other curves like $|V_{m2}|$.

Comparing Fig. 11a and 11b, we can see that the height of the right peaks depends on the sound frequency. The higher the frequency, the lower the peaks. This is explained by the fact that the density of Brillouin rays is higher at higher frequencies. The same scattered energy in a given angular sector around the critical angle is distributed over a larger number of Brillouin rays (or modes) contained in that sector.

We considered both normal modes and quasi-modes in constructing Fig. 11. For 137 Hz, 4 modes were calculated (Fig. 11a). Among them, mode 1 is a normal mode in the whole range from 100 to 2400 m s^{-1}. Modes 2, 3, and 4 are quasi-modes within the respective intervals 896–1480, 637–1610, and 488–1894 m s^{-1} (and normal modes beyond these intervals). For 250 Hz, 7 modes were considered (Fig. 11b). Of these, modes 1–5 are normal modes over the whole range considered. Modes 6 and 7 are quasi-modes within the intervals 998–1168 and 889–1157 m s^{-1}, respectively. It can be seen from Fig. 11 that, as c_1 changes, the transition from the normal mode state to the quasi-mode state is in no way reflected in the shape of the curves.

The curves in Fig. 11 were calculated for the gradient $c_1' = 0.23$ s^{-1}. There are no qualitative changes in Fig. 11 for any gradient: for larger c_1', the curves will be higher than in Fig. 11, and they will be lower if the gradient is smaller. This circumstance allows us to use Fig. 11 to estimate mode coupling in other, more realistic, situations.
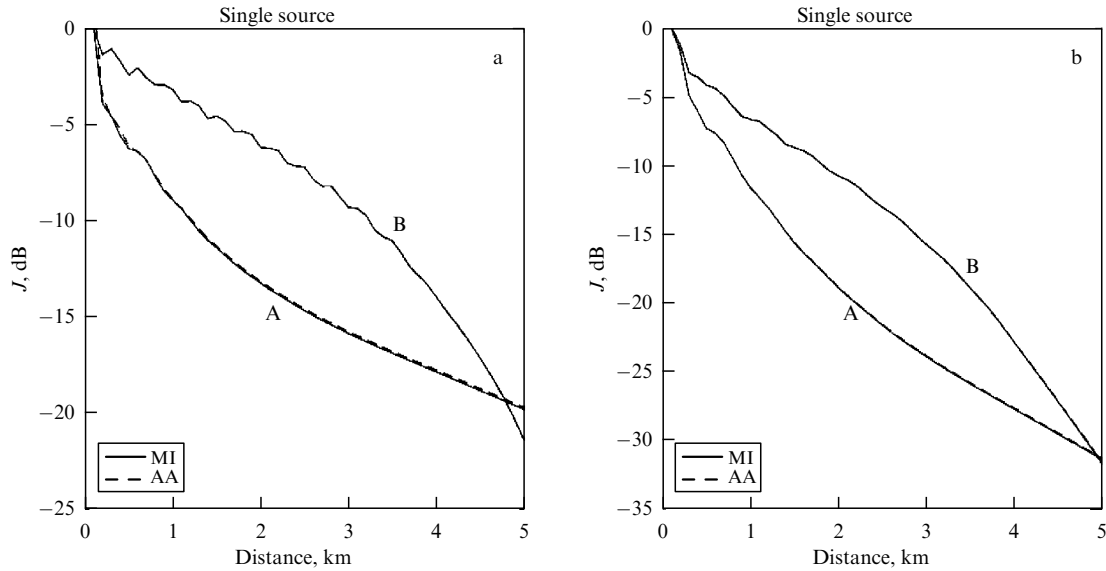
Figure 12. Attenuation curves taking into account mode coupling (MI, solid lines) and in the adiabatic approximation (AA, dashed lines) for a single source for direct (A) and inverse (B) propagation on path 4. Solid and dashed lines practically coincide. (a) $f = 137$ Hz, (b) $f = 250$ Hz.

5.2 Mode coupling in estimates of sound attenuation in a waveguide with an inhomogeneous bottom

As an example, consider a sound field from a point source located at depth $z_0 = 14$ m on track 4 shown in Figs 3 and 9. Simulations use formula (15), which accounts for mode coupling. To estimate their effect, the attenuation curves $J(r)$ obtained using (15) and (9) are compared with the results of simulations $J(r)$ based on formulas (11) and (9) in the adiabatic approximation.

In Fig. 12, we present the dependences of $J(r)$ for a single source and sound propagation on track 4 from the left to right (direct radiation) and in the opposite direction, from right to left (inverse radiation). Practically ideal agreement between the curves with and without consideration of mode coupling is observed (the solid and dashed lines are very close). An important ensuing conclusion is that the decay with distance of the mean intensity of the sound field emitted by a point source bears an adiabatic character in a shallow water with an inhomogeneous bottom. This does not exclude the effect of mode coupling on individual waveguide modes (see [41] and Section 7 for more details).

6. Horizontal refraction of sound waves in a waveguide with an inhomogeneous bottom structure

All the situations considered above are in fact two-dimensional (or have a cylindrical symmetry) in the coordinates (r, z) — the distance–depth, i.e., in the vertical plane. Solutions (4), (11), and (15) for the complex amplitude of a sound field can be generalized to the three-dimensional case, which includes the angular coordinate φ in the horizontal plane if the sound propagation along different directions φ can be considered independent. This is known as the $N \times 2D$ approximation, or the approximation of uncoupled azimuths, where N is the number of directions [40]. This approximation, however, does not work in the presence of three-dimensional effects, e.g., when the propagation direction changes due to refraction of sound waves in the horizontal plane.

To analyze possible three-dimensional effects associated with the inhomogeneous structure of the bottom, the contributions of each waveguide mode are considered separately, assuming that the modes are adiabatic. The resulting field at a given point in the waveguide can be conveniently written in the Cartesian frame of reference (x, y, z) and, by analogy with (4), expanded in the sum of local modes $\psi_m(\mathbf{r}, z)$,

$$P(\mathbf{r}, z) = \sum_{m=1}^{M} P_m(\mathbf{r}, z) = \sum_{m=1}^{M} A_m(\mathbf{r}; z_0)\psi_m(\mathbf{r}, z), \qquad (26)$$

where $\mathbf{r} = (x, y)$ is the radius-vector of a point in the horizontal plane, and the modal amplitude $A_m(\mathbf{r})$ satisfies the equation

$$\Delta_r A_m(\mathbf{r}) + \xi_m^2(\mathbf{r})A_m(\mathbf{r}) = 0. \qquad (27)$$

Here, $\xi_m(\mathbf{r}) = q_m(\mathbf{r}) + \mathrm{i}\gamma_m(\mathbf{r})/2$ is the complex propagation constant of the mth mode, and $\Delta_r = \partial^2/(\partial x^2) + \partial^2/(\partial y^2)$ is the Laplace operator. The initial condition is defined by the excitation coefficient of the given mode: $A_m(\mathbf{r} = 0) \sim \psi_m(\mathbf{r} = 0, z_0)$, where z_0 is the depth of the sound source.

We consider several lower modes, as only they contribute significantly in the resulting field. The local propagation constants $\xi_m(\mathbf{r})$ and the profiles of the modes $\psi_m(\mathbf{r}, z)$ are defined by expression (6).

To calculate the modal amplitudes $A_m(\mathbf{r})$, equation (27) is reduced to a parabolic equation [42] by considering only forward scattering and using the Padé approximation for the square root operator

$$\frac{\partial A_m}{\partial x} = \mathrm{i}q_l^0 \left(1 + \sum_{j=1}^{n} \frac{a_{j,n} X_m}{1 + b_{j,n} X_m}\right) A_m. \qquad (28)$$

The expansion coefficients $a_{j,n}$, $b_{j,n}$ are chosen to ensure stability and the required accuracy of the solution:

$$X_m = q_m^{0 \, -2}\left(\frac{\partial^2}{\partial y^2} + \xi_m^2 - q_m^{0 \, 2}\right),$$

where q_m^0 is the real part of the horizontal wavenumber of the mth mode at the source point. The numerical solution of the differential equation can be obtained with the help of the split-step Padé algorithm [43]. Here, it is assumed that the sound waves propagate predominantly in some angular sector around the x-axis direction, and that the gradients of the waveguide parameters are mostly parallel to the y-axis.

To estimate the sound attenuation with distance, we calculate the depth-averaged intensity levels in the horizontal plane for individual modes,

$$\tilde{J}_m(\mathbf{r}) = 20 \lg \frac{|A_m(\mathbf{r})|}{|A_m(\mathbf{r}_0)|} , \qquad (29)$$

and for the full field,

$$\tilde{J}(\mathbf{r}) = 10 \lg \frac{\int_0^H |P(\mathbf{r}, z)|^2 \, \mathrm{d}z}{\int_0^H |P(\mathbf{r}_0, z)|^2 \, \mathrm{d}z} . \qquad (30)$$

The reference point $\mathbf{r}_0$ is placed at a distance $|\mathbf{r}_0| = 100$ m along the axis X. The field at $|\mathbf{r}| \geqslant |\mathbf{r}_0|$ is determined by the discrete spectrum of the modes, and the continuous spectrum can be ignored. Note that, unlike formula (9), there is no additional compensation for the cylindrical divergence of the sound wave front.

In the following, we consider in detail two models of an inhomogeneous bottom: (1) an idealized model in which it is assumed that the sound speed depends only on one, horizontal, coordinate; (2) a model that is as close as possible to a realistic case, constructed on the basis of 3D seismic surveying data in the Kara Sea (for details, see [29]).

## 6.1 Idealized waveguide with a linear profile of sound speed in the bottom

Let us consider the idealized shallow-water waveguide shown in Fig. 13, which represents a homogeneous water layer of constant thickness $H = 28$ m over an inhomogeneous bottom half-space.

We analyze the sound field in a transitional region from an acoustically soft bottom ($c_1 < c$) to an acoustically hard bottom ($c_1 > c$). The sound speed in the bottom varies in a piecewise-linear fashion along the y-axis, but is independent of the coordinates x and z:

$$c_1(y) = \begin{cases} 1400 \text{ m s}^{-1} & \text{for } y < -1000 \text{ m (soft bottom)} , \\ (1500 + 0.1y) \text{ m s}^{-1} & \text{for } -1000 < y < 1000 \text{ m} , \\ 1600 \text{ m s}^{-1} & \text{for } y > 1000 \text{ m (hard bottom)} . \end{cases}$$

To limit the domain in which equation (28) is integrated, artificial sponge layers are introduced for $y < -2000$ m and $y > 2000$ m.

Figure 14 shows the dependences of the phase speed $V_m^{\mathrm{ph}} = \omega/q_m$ and the attenuation coefficient $\gamma_1/2$ of the first mode of the sound speed in bottom c_1 computed for the set of frequencies f: 29, 55, 81, 108, and 134 Hz. (For the sake of demonstration, we deliberately took a wider range for the variation in the sound speed in the bottom than in the explored transitional region; its limits are marked by two vertical dashed lines.) It can be seen that the phase speed in this region has a global minimum, which is deeper for a lower frequency. By placing the transducer close to this minimum, one can expect to see manifestations of horizontal refraction. It should also be noted that the mode attenuation drops by
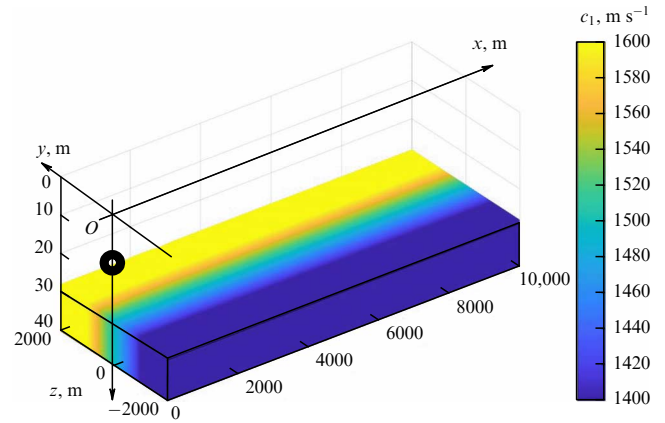

Figure 13. Schematics of model waveguide with the distribution of sound speed in a bottom in the transitional region from an acoustically soft to an acoustically hard bottom. Black circle indicates the position of the source in simulations.
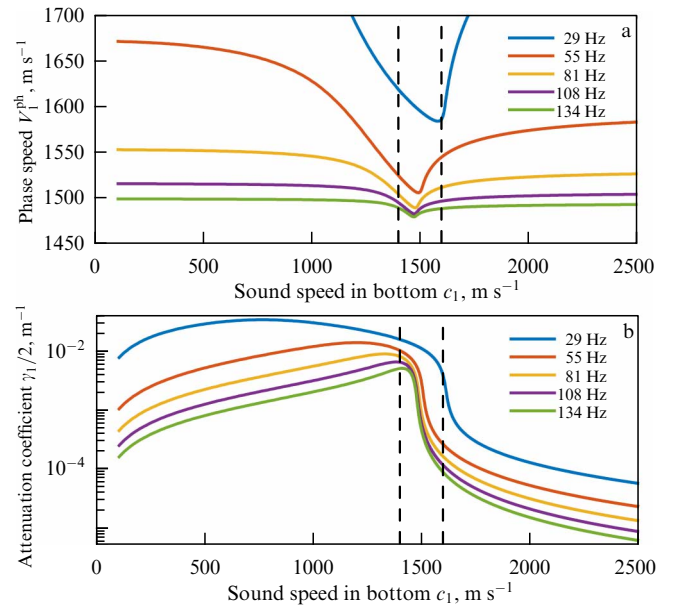

Figure 14. Dependence of (a) phase speed and (b) attenuation coefficient of the first mode on the sound speed in bottom. Vertical lines mark the boundaries of transitional domain.

approximately two orders of magnitude on passing from an acoustically soft to an acoustically hard bottom. This peculiarity should be taken into account when solving equation (28). Similar behavior is observed for modes with other numbers.

The sound field is calculated for a sound source placed at the depth $z_0 = 15$ m in the center of the transition region, i.e., in the immediate vicinity of the minimum of the phase speed. To illustrate the three-dimensional effect, a frequency of the 55 Hz is chosen, at which the sound field is effectively formed by only one (the first) waveguide mode. Figure 15 presents the dependence of the mode phase speed on the coordinate y and shows the modal ray trajectories in the horizontal plane. As can be seen, when the source is placed close to the local minimum, the rays deviate from straight lines — they are horizontally refracted. Maximum refraction angles reach $7.5°$. (The refraction angle is the angle between the straight line connecting the source and the receiver and the ray arriving at the receiver.)
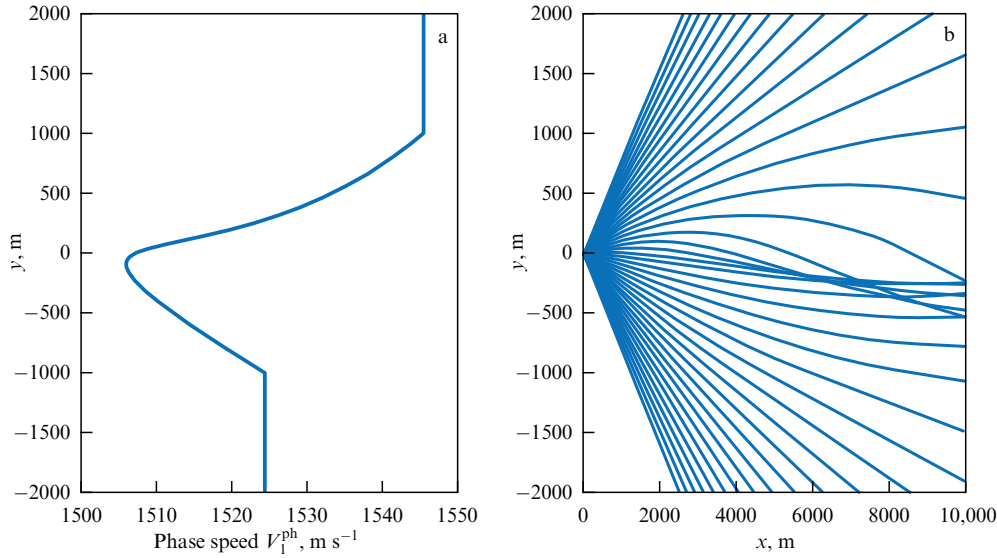
Figure 15. (a) Spatial dependence of phase speed of the first mode at a frequency of 55 Hz and (b) respective trajectories of modal rays in horizontal plane for sound source placed at center of transitional domain.
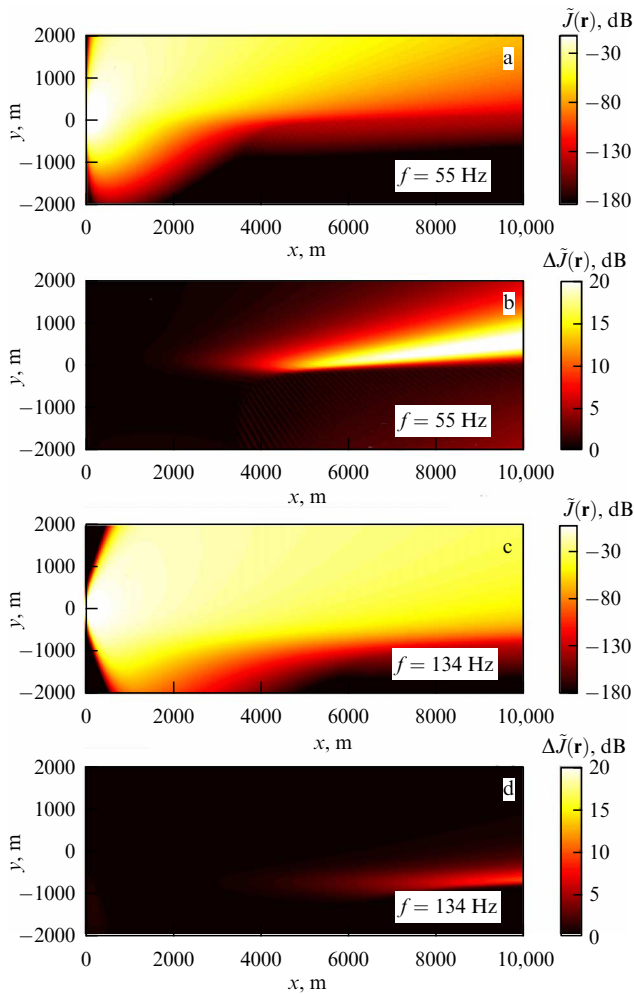
Figure 16. Two-dimensional distribution of depth averaged sound intensity levels $\tilde{J}(\mathbf{r})$ in horizontal plane at frequencies of (a) 55 Hz and (c) 134 Hz; difference in levels $\Delta\tilde{J}(\mathbf{r})$ calculated with and without accounting for horizontal refraction for frequencies of (b) 55 Hz and (d) 134 Hz.

Let us see how much the curvature of the modal trajectories affects the energy redistribution in the horizontal plane. The distribution of the relative intensity level $\tilde{J}(\mathbf{r})$ in the plane (x, y) is shown in Fig. 16a. Note that, in this case, $\tilde{J}(\mathbf{r}) \approx \tilde{J}_1(\mathbf{r})$, where $\tilde{J}_1$ is the sound field level in the first mode (29). The first thing we notice is a strong anisotropy in the intensity decay as a function of the selected direction, which is explained by significant spatial variability in the attenuation coefficient and is not related to horizontal refraction. To isolate the effect of refraction proper, the level $\tilde{J}(\mathbf{r})$ is compared with the level $\tilde{J}_0(\mathbf{r})$ computed in the uncoupled azimuth approximation (the $N \times 2D$ approximation). The spatial distribution of the difference in intensity levels $\Delta\tilde{J}(\mathbf{r}) = \tilde{J}(\mathbf{r}) - \tilde{J}_0(\mathbf{r})$ is shown in Fig. 16b. It can be seen that, due to the horizontal refraction, there is an additional insonification of part of the bottom transitional region. The explanation is that a curved ray, despite its larger trajectory length, travels a shorter distance in the region of strong attenuation than a direct ray does. The maximum increase in the amplitude under the given conditions reaches $\Delta\tilde{J}_{max} = 22$ dB.

Moving to higher frequencies and a multimodal regime, the effect of refraction for the first mode weakens, yet becomes expressed for other modes, which, however, decay more strongly [28]. Figure 16c shows the results of computations for a frequency of 134 Hz, when the field is composed of three modes. Due to the dominance of the first mode in the total field, the maximum difference in levels between the three-dimensional case and the $N \times 2D$ approximation does not exceed $\Delta\tilde{J}_{max} = 12$ dB (Fig. 16d).

The simulations show that, after moving the source with a frequency of 134 Hz relative to the position where the phase speed of the first mode is minimum by 500 m in a positive or negative direction along the y-axis, $\Delta\tilde{J}_{max}$ decreases to 6 dB. At a frequency of 55 Hz, the width of the source region for which the reduction in the level difference $\Delta\tilde{J}_{max}$ exceeds 6 dB with respect to maximum is about 2000 m.

It should be noted that such effects of horizontal refraction can, in principle, be observed not only at the transition from acoustically soft to acoustically hard bottom but also, for
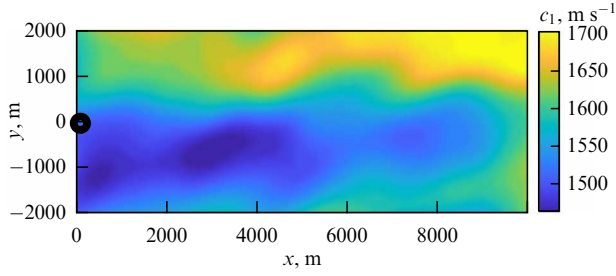
Figure 17. Sound speed field in a horizontal section at a depth of 41 m relative to the waveguide upper boundary in the rectangular domain shown by dotted lines in Fig. 3a. Black circle shows the position of transducer used for modeling.
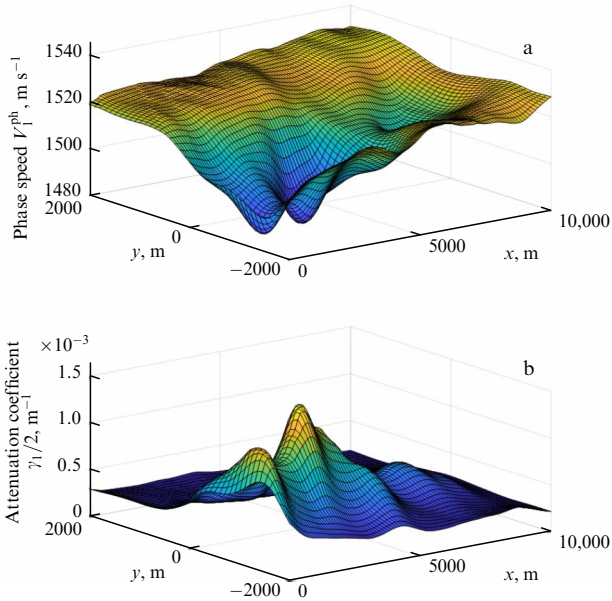
Figure 18. Spatial distribution of (a) phase speed and (b) attenuation coefficient of the first mode at a frequency of 55 Hz.

example, when hard bottom regions with different sound speeds, close to the sound speed in water, follow each other.

6.2 Shallow-water waveguide with an inhomogeneous bottom

Simulations of transmission loss based on the simplified waveguide model show that horizontal refraction can occur in a shallow water waveguide in a transitional region between an acoustically soft and hard bottom even if the water layer thickness is uniform. But a question arises: do such regions exist in nature? In order to observe refraction, the transitional region should not only be sufficiently long (several km in length) but also have a sufficiently uniform interface.

An example of a shallow water waveguide with a constant water layer thickness can be given by some regions of the Kara Sea (see Fig. 3). To study the three-dimensional effects in the propagation of sound waves, we selected a rectangular region of the seafloor, marked by dashed lines in Fig. 3a and shown separately in Fig. 17, where the strongest sound speed gradients are observed, while the sound speed is close to that in water (a water-like bottom). From the data shown in Fig. 17, it can be seen that the sound speed in the bottom c_1 varies from 1460 m s^{-1} (blue regions) to 1700 m s^{-1} (yellow regions).

The distributions of the phase speed V_1^{ph} and attenuation coefficient $\gamma_1/2$ of the first mode at a frequency of 55 Hz
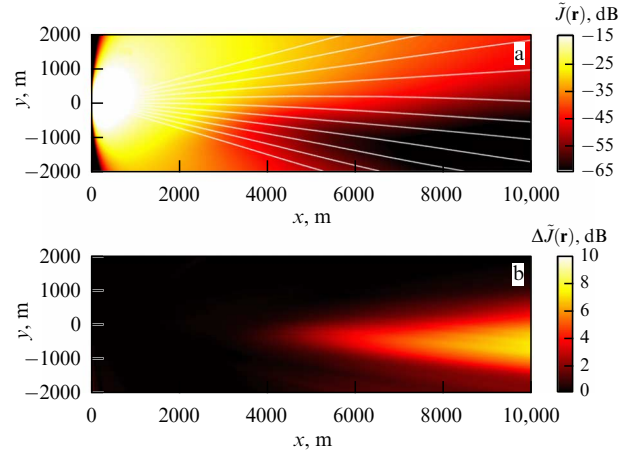
Figure 19. (a) Two-dimensional distribution of level of depth-averaged intensity $\tilde{J}(\mathbf{r})$ in horizontal plane at a frequency of 55 Hz with superimposed trajectories of modal rays of the first mode. (b) Difference in transmission loss calculated with and without accounting for horizontal refraction.

calculated for the selected region are shown in Fig. 18. Figure 18a clearly shows a strong spatial variability of the modal phase speed in the region of a low-speed bottom. The gradient of phase speed at the boundary of the region reaches 0.06 (m s^{-1}) m^{-1}. The highest values of modal attenuation are also observed in this region (up to 1.5×10^{-3} m^{-1}, or 13 dB km^{-1}).

The canyon-like distribution of the phase speed in Fig. 18a leads to the effect of horizontal refraction, which is demonstrated in Fig. 19 for a source located at the point with coordinates $x = 0$, $y = 0$. As in the case of an idealized waveguide model, attention is drawn to the curved modal ray trajectories in the horizontal plane, shown by white lines in Fig. 19a. The maximum refraction angle in this case is 6°. The maximal difference in the levels of depth-averaged intensity in the horizontal plane $\Delta\tilde{J}_{\max}$, calculated with and without taking the horizontal refraction into account, is found in the region where the sound speed in the bottom is low and is equal to 7 dB. Note that if the source is moved to the point with the coordinates $x = 0$, $y = -1000$ (in the middle of the 'canyon'), the level difference reaches 10 dB. If the sound frequency is increased to 134 Hz, this difference decreases to 4 dB.

7. Manifestation of the effects of mode coupling and horizontal refraction for broadband signals

All the results presented above refer to tonal acoustical signals. It may be interesting to study the effects discussed above for a broad frequency band and for pulse signals. This is important, for example, for a more accurate prediction of the acoustical impact on underwater animals at low frequencies [44] and for estimating the feasibility of underwater acoustical communication at higher frequencies [45]. A typical low-frequency broadband source (30–80 Hz) is an airgun used for seismic survey (see, e.g., [46]). The most promising range for long-distance underwater acoustical communication on the shallow-water Arctic shelf is the 500–1000 Hz interval.

Modeling of broadband signals in complex waveguides was carried out in Refs [47–49], but three-dimensional

inhomogeneities in the bottom were only considered in [31]. References [31, 50, 51] show in the framework of numerical modeling that the frequency dependence of modal amplitudes due to mode coupling on a compact irregularity (local bottom feature, an internal wave soliton, ice keel, etc.) gets characteristic modulation with a period depending on the distance to the irregularity. By measuring the period of this modulation, one can estimate the distance from the sound source to the irregularity on a stationary acoustic track.

We further consider the formation of a broadband acoustic field by an omnidirectional source in the frequency range of 35 to 1000 Hz in a shallow water waveguide with a constant depth but an inhomogeneous sound speed structure in the upper sediment layer (see [31, 50, 51] for details). As in Section 6, two models of bottom are chosen, one ideal and one realistic. Mode coupling are analyzed for sound propagation across the inhomogeneity, and horizontal refraction is analyzed for propagation along the inhomogeneity. The first effect is more pronounced at higher frequencies (100–1000 Hz), and the second one is better seen at low frequencies (up to 100 Hz) in a single mode regime.

The Green's function of problem (3) for different frequencies $\omega = 2\pi f$ will be denoted as $P(\omega, x, y, z)$. It is calculated according to (15) or (26) for individual frequency components with a step of 1 Hz in the frequency band $f = 35$–1000 Hz. Calculations of $P(\omega, x, y, z)$ in the case of mode coupling can be conveniently performed using the wide-angle parabolic equation with subsequent mode isolation on a vertical array [43].

Let $S_0(\omega)$ be the spectrum of an emitted signal, defined as an additional multiplier on the right-hand side of the Helmholtz equation (3). In this case, the spectrum of the received signal is $S(\omega, x, y, z) = S_0(\omega) P(\omega, x, y, z)$. After matched filtering with the emitted signal, the temporal realization of the received signal at the output of the correlation receiver is obtained by Fourier synthesis

$$u(t, x, y, z) = 2 \operatorname{Re} \left\{ \int_0^\infty |S_0(\omega)|^2 P(\omega, x, y, z) \exp(-\mathrm{i}\omega t) \, \mathrm{d}\omega \right\}. \tag{31}$$

For the sake of simplification, it is assumed in this work that the emitted signal has a uniform spectrum $|S_0(\omega)| = 1$ in the range of 35–1000 Hz. With a high degree of accuracy, this corresponds to a signal with linear frequency modulation (LFM).

The amplitude of the signal at the output of the correlation receiver will be presented on a logarithmic scale (in dB),

$$\mathrm{SL}(t, x, y, z) = 20 \lg \left(\frac{u_{\mathrm{envel}}(t, x, y, z)}{\max_t u_{\mathrm{envel}}(t, x = 1\,\mathrm{m}, 0, 0)} \right), \tag{32}$$

where $u_{\mathrm{envel}} = |\dot{u}|$ is the envelope of the signal u obtained as the absolute value of the analytical signal $\dot{u} = 2 \int_0^\infty |S_0|^2 P \exp(-\mathrm{i}\omega t) \, \mathrm{d}\omega$.

We describe the technique of approximate isolation of the modal amplitudes A_m from the spectrum of the signal u, i.e., from $U = |S_0|^2 P$, with the aid of a vertical receiving array passing through the entire water layer column. From (15) or (26), we have $U = |S_0|^2 \sum A_n \psi_n$. We replace the exact orthogonality condition for eigenfunctions (17) with an approximate one, $\int_0^H \psi_m \psi_n \mathrm{d}z \approx \delta_{mn}$. We multiply the first equality by ψ_m and integrate from 0 to H. It follows that

$|S_0|^2 A_m \approx \int_0^H U \psi_m \, \mathrm{d}z$. In practice, if the source spectrum is not corrected, the product is $|S_0|^2 A_m$. In our theoretical analysis, taking into account the unity spectrum of the source, we find

$$A_m(\omega, x, y) \approx \int_0^H P(\omega, x, y, z) \psi_m(\omega, x, y, z) \, \mathrm{d}z. \tag{33}$$

In the following, we will only give absolute values of (33), i.e., $|A_m(\omega, x, y)|$.

7.1 Idealized waveguide
### with a linear sound speed profile in the bottom
We begin with an idealized model of shallow water waveguide shown in Fig. 13. There is a water layer of constant thickness H and a constant sound speed c on an inhomogeneous bottom half-space. The width Δy of the transitional region between acoustically soft and hard bottom types varies in the range from 600 to 4000 m.

Interaction of modes. To study the details of mode coupling, an acoustical track of length of $r = 4$ km is oriented along the y-axis. A sound source is located at a point with the coordinates $x_0 = 4000$ m, $y_0 = 2000$ m at depth $z_0 = 10$ m. A vertical receiving array, which filters modes using (34), traverses the entire waveguide depth with a step of 1 m at a point $x_A = 4000$ m, $y_A = -2000$ m. Modal filtering (33) shows that the sound field at the end of the acoustical track is dominated mainly by the first, most energetic mode. This is caused by a strong increase in modal attenuation with the mode number in the region of the low-speed bottom.

Figure 20 presents frequency dependences for the amplitude of the first mode at the receiving array for different sizes Δy of the transitional domain. It can be seen that the frequency dependence of the first mode amplitude in the case of sound propagation over the inhomogeneous bottom contains oscillations whose amplitude increases as the width of the inhomogeneity Δy decreases. The appearance of the modulation is the consequence of mode coupling and serves as an indicator of the presence of inhomogeneities in the bottom structure. This effect is pronounced at frequencies above 200 Hz. In the absence of bottom
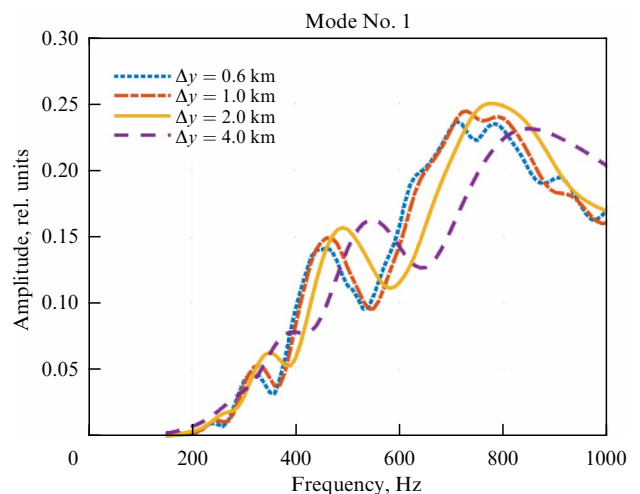
Figure 20. Frequency dependence of the first mode amplitude in a waveguide with a linear sound speed profile in the bottom for various sizes of transitional region Δy.
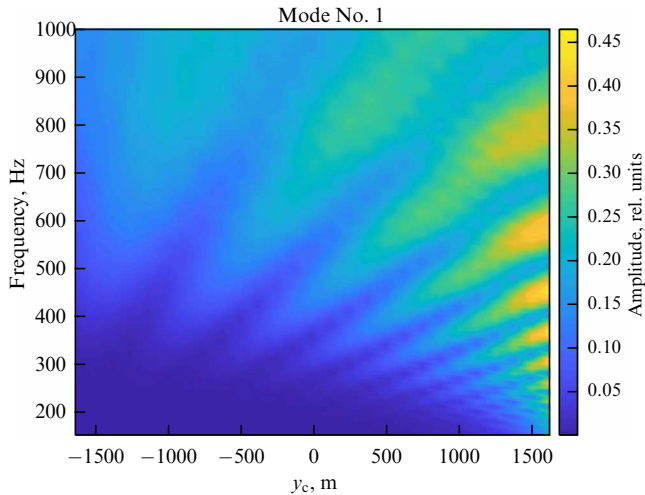
Figure 21. Frequency modulation of the amplitude of the first mode depending on the shift of the center of transitional region y_c. Width of transitional region is fixed: $\Delta y = 600$ m.

inhomogeneities, the first mode amplitude is a monotonic function of frequency.

Fixing the track length to $r = 4$ km and the length of the transitional region to $\Delta y = 600$ m and varying only the position of the center of this region y_c, one can find that the period of modulation varies approximately 7-fold (Fig. 21). Moreover, the frequency period of oscillations depends uniquely on the distance between the sound source and the bottom inhomogeneity, which can be used to localize this inhomogeneity [50].

The following remark should be made here. It has been shown in Refs [50, 51] that such a modulation in the frequency domain should accompany the mode coupling only on a compact inhomogeneity (a local irregularity in the relief, a separate ice keel, a soliton of internal waves), the size of which is smaller than the period of the interference beat of the first and second modes. The inhomogeneity, in the form of a transitional region between different bottom types, does not satisfy the compactness criterion. However, as mentioned in Section 5, intense interaction between the first and second modes takes place only on that part of the acoustic track where the sound speed in the bottom c_1 is approximately equal to the sound speed in the water layer c: outside this part the mode coupling is negligibly small. Taking this detail into account, the inhomogeneity considered by us can be seen as compact. The same can explain the shift of the dependences along the frequency axis in Fig. 21. The change in the width of the transitional region Δy leads to a change in the distance from the sound source to the track point where $c_1 \approx c$. For $\Delta y = 600$ m, this point is located at a distance of 2090 m, and for $\Delta y = 4000$ m, at a distance of 2600 m.

Horizontal refraction. In the framework of the study of horizontal refraction, the sound source was placed in the center of the transitional region at the point with coordinates $x_0 = 0$, $y_0 = 0$ at the depth $z_0 = 15$ m. An analysis of the sound field was carried out mainly at the location of a vertical array which was placed at distance $r = 10$ km from the source at the point $x_A = 10{,}000$ m, $y_A = 0$.

In studies of horizontal refraction, we are most interested in the frequency range up to 100 Hz, where the manifestations of this effect are maximal. At such frequencies, there is only one energy carrying mode in the waveguide, i.e., a one-mode regime is realized. The dependence of the group and phase velocities of the first mode, as well as its attenuation coefficient, on the sound frequency and the sound speed in the bottom are shown in Fig. 22. We note that the group velocity V_1^{gr} has a global minimum at frequencies of 50–100 Hz (Fig. 22a), which is located in the region where the sound speed in the bottom c_1 is close to that in the water c. This is closely related to the presence of a minimum of the phase speed V_1^{ph} in the same region. In Section 6, we mentioned that the placement of a point tonal transducer in this region leads to horizontal refraction.
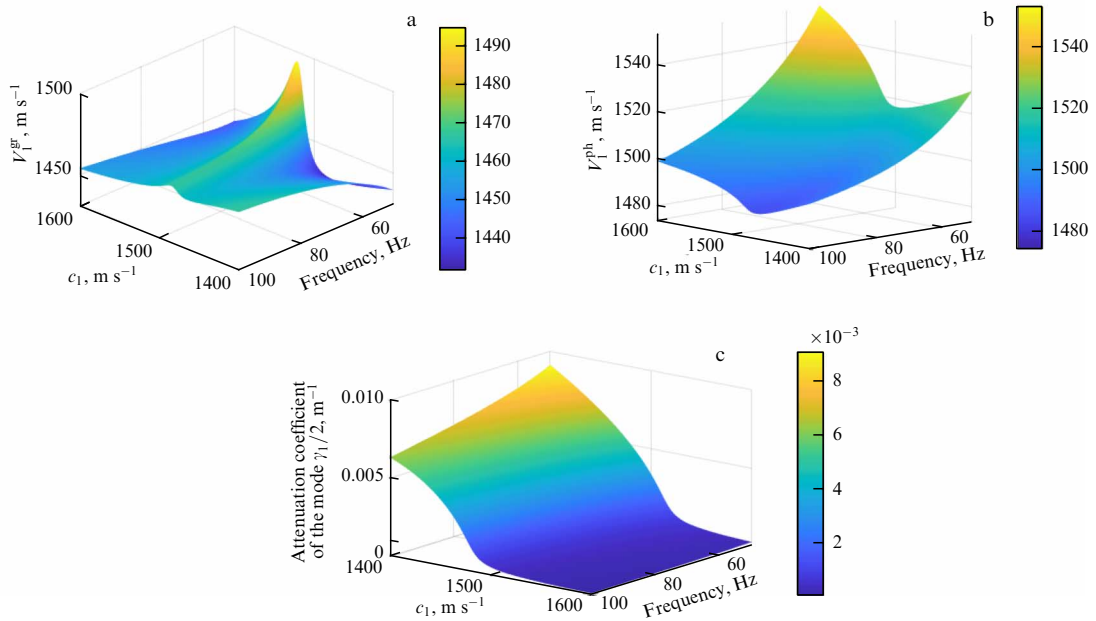
Figure 22. Dependence of (a) group velocity, (b) phase speed, and (c) attenuation coefficient of the first mode on source frequency and sound speed in the bottom.
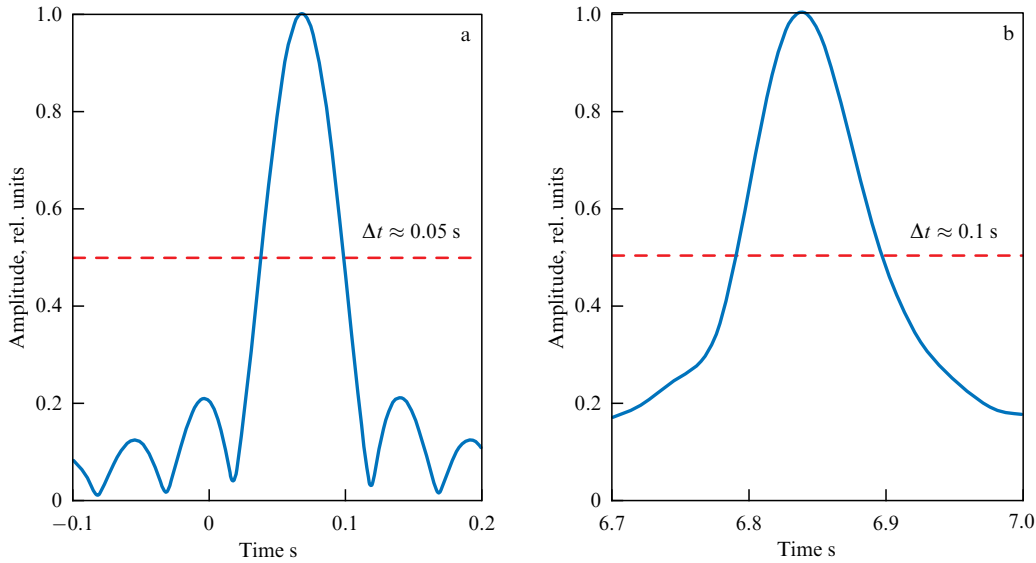
Figure 23. Envelopes of the received pulse normalized by the maximum value at distance (a) $x = 100$ m and (b) $x = 10{,}000$ m from the source along line $y = 0$. Width of transitional region $\Delta y = 2000$ m.
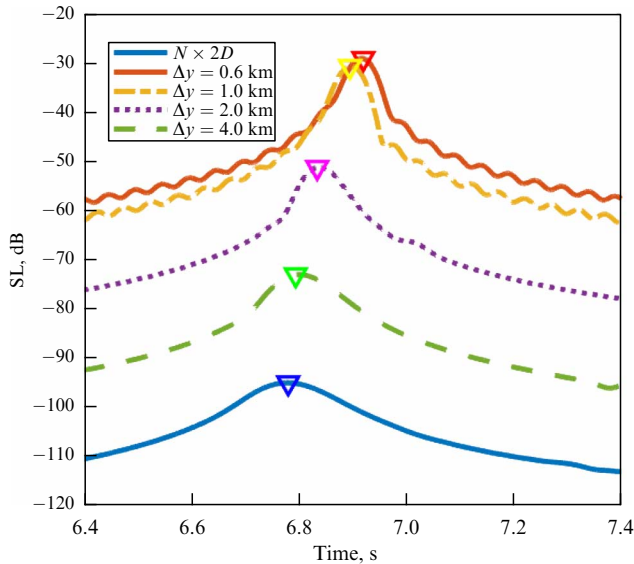
Figure 24. Envelopes of received pulse on a logarithmic scale at distance $x = 10{,}000$ m from the source for $y = 0$ and different transverse sizes of transitional region Δy. Lower blue curve is calculated without taking into account horizontal refraction in the $N \times 2D$ approximation. Triangles show the positions of maxima.

The effect of horizontal refraction for a broadband signal can be demonstrated by analyzing a low-frequency acoustical pulse obtained as the output of a correlation receiver (31). Since the refraction effect is more pronounced at lower frequencies and bottom absorption increases significantly (Fig. 22c), the frequency range of 50–70 Hz was chosen for studies, for which the loss accompanying sound propagation are still moderate. It is important to note that this range is most relevant for seismic studies of the sea bottom, as it contains a dominant fraction of the energy of an airgun [46].

Figure 23 shows the pulse envelopes normalized with the maximum value, $u_{\text{envel}}(t, x, y, z) / \max_t u_{\text{envel}}(t, x, y, z)$, at points $x = 100$ m and 10 km from the transducer for propagation along the straight line $y = 0$ and for the fixed transverse size of the transitional region $\Delta y = 2000$ m between acoustically soft and acoustically hard bottom

types. It can be seen that, as the pulse propagates, its width doubles at the 0.5 level (from 0.05 s to 0.1 s) due to the frequency dependence of the attenuation coefficient of the first mode and its intramodal dispersion.

Figure 24 shows envelopes of the pulses on a logarithmic scale $SL(t, x, y, z)$ for transitional regions of different transverse sizes Δy. The pulses were calculated using the modal parabolic equation method as well as the uncoupled azimuth approximation (the $N \times 2D$ approximation), when the horizontal diffraction is ignored, and the modeling is performed independently for different vertical slices of the waveguide. The following conclusions can be drawn from Fig. 24.

(1) The maximum amplitude $SL_{\max}(x, y, z) = \max_t SL(t, x, y, z)$ of a low-frequency pulse increases by up to 65 dB compared to the $N \times 2D$ approximation due to horizontal refraction, which occurs because the pulse propagating along a curved trajectory passes over the bottom where sound attenuation is smaller. The effect of the width of the transition region Δy on the magnitude of $SL_{\max}$ is only noticeable up to a certain limit value $\Delta y \approx 1.0$ km.

(2) As Δy decreases, the pulse propagation time increases, indicating significant horizontal refraction. The delay of arrival is 0.1 s for a distance of 10 km when the width of the transitional region is $\Delta y \approx 1.0$ km.

7.2 Shallow water waveguide with an inhomogeneous bottom

To study the manifestations of mode coupling and horizontal refraction in a realistic waveguide model with an inhomogeneous bottom structure, we selected the same region as in Section 6.2 (see Fig. 17).

Mode coupling. To analyze the mode coupling, we took a vertical waveguide section along the y-axis for $x = 3500$ m, shown separately in Fig. 25a. The sound source depth is $z_0 = 5$ m. The length of the acoustic track is $r = 4$ km. Unlike the ideal waveguide model discussed above, here, the sound speed in the bottom c_1 does not fall below the sound speed in water c. In addition, the sound source and the receiving array are located above an acoustically hard bottom. These two factors imply the presence of several energy carrying modes at frequencies below 1 kHz.
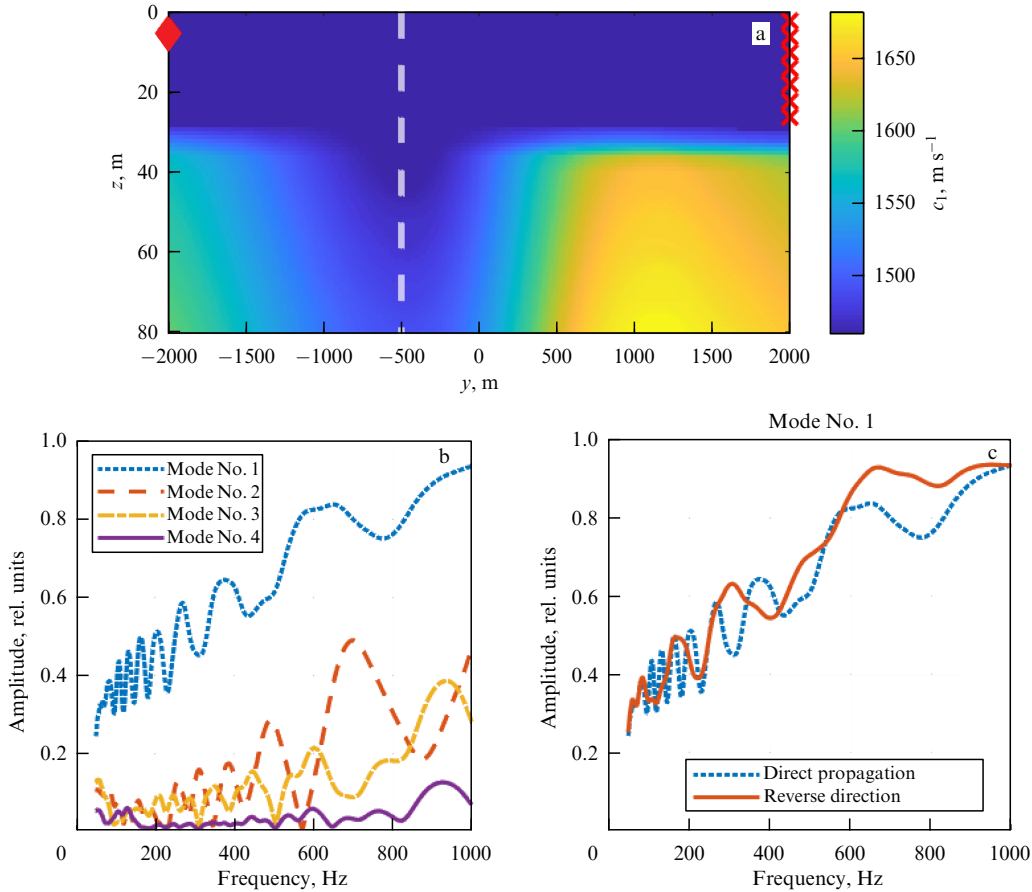
Figure 25. (a) Sound speed along an acoustical track; white dashed line marks position of sound speed minimum in the bottom; (b) frequency dependence of modal amplitudes of first four modes on a vertical array; (c) frequency dependence of amplitude of first mode at the distance of 4 km for sound propagation in direct (from left to right) and reversed (from right to left) directions. Red rhombus shows source position, red chain shows position of receiving array.

The frequency dependence of the amplitudes of the first four modes is shown in Fig. 25b. It can be seen that the main contribution to the sound field comes from the 1st, 2nd, and 3rd modes, while their amplitudes show significant oscillations in the frequency domain. This is the result of mode coupling. Figure 25c presents the frequency dependences of the first mode amplitude for the direct (from left to right) and reversed (from right to left) orientations of the acoustical tracks. As can be seen, the period of oscillations is very different, which is most evident at frequencies below 500 Hz.

The region of the low-speed bottom is located approximately in the middle of the acoustical track, closer to the sound source: the minimum of the sound speed in the bottom is located at $y = -500$ m (Fig. 25a). As for the idealized bottom model, this region can be considered a compact inhomogeneity. In a waveguide with a constant sound speed in water, the distance r_s from a sound source to a compact inhomogeneity is directly proportional to the number L of the first mode amplitude maxima that occur in a fixed frequency band, i.e., $r_s \sim L$ [50]. This fact can be used to localize the inhomogeneity. We skip the solution to the problem of the proportionality factor between r_s and L and use the following approach. Denote by L the number of maxima for the direct track orientation, and by L' the inverse one. The distances from the source to the inhomogeneity are denoted as r_s and r_s', respectively, and $r_s + r_s' = r$ is the total acoustical track length. In this case, the relation $r_s'/r_s = L'/L$ will hold , or $(r - r_s)/r_s = L'/L$, from which the distance to the inhomo-

geneity can be estimated as $r_s = r/(1 + L'/L)$. The ratio $L'/L \approx 2$ for frequencies below 500 Hz, taking into account the track length $r = 4000$ m, gives the distance from the source to the inhomogeneity $r_s \approx 1330$ m. This value coincides up to 170 m with the position of the sound speed minimum in the bottom, which is marked by the horizontal dashed line in Fig. 25a.

Horizontal refraction. To demonstrate horizontal refraction, a sound source is placed at point $x_0 = 0$, $y_0 = 0$, $z_0 = 15$ m (as in Section 6.2), and a vertical receiving array is placed at point $x_A = 10{,}000$ m, $y_A = 0$. Figure 26a shows a horizontal section of the sound speed field in the bottom at a depth of 14 m relative to the water–bottom interface, with the source and array positions indicated. The pulses simulated for the frequency range from 35 to 65 Hz are shown in Fig. 26b–d. The sound field at these frequencies is formed by only one energy-carrying mode.

As in the case of an idealized model waveguide, an increase in the level SL (Fig. 26b) is observed at the receiver point at a distance of 10 km, calculated with the horizontal refraction taken into account, compared to the case where horizontal refraction is disregarded ($N \times 2D$ approximation). The difference between the maximum levels is $\Delta SL_{max} \approx 11$ dB. The delay in the arrival time of a pulse signal is about $\Delta t = 0.1$ s. These effects are manifestations of horizontal refraction.

Figure 26c, d shows how the pulse duration changes as the pulse travels along the acoustical track. The pulse width at the
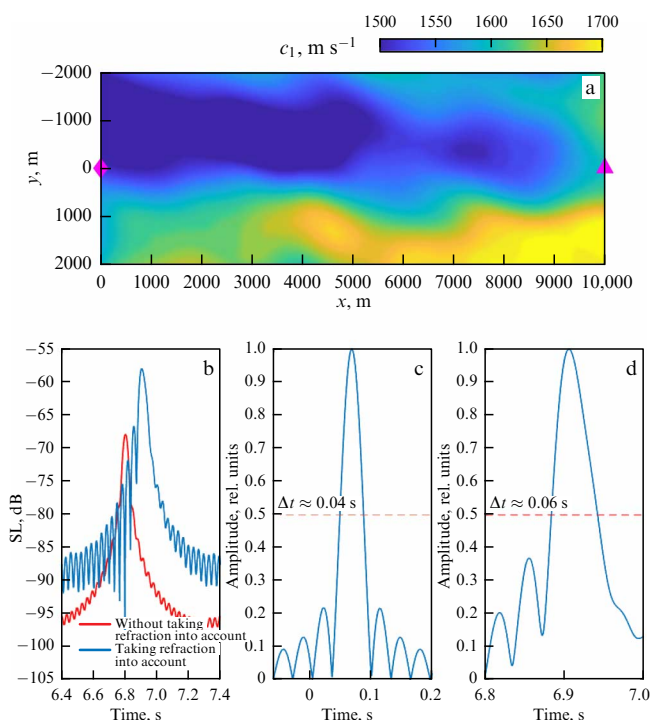
Figure 26. (a) Horizontal section of the field of sound speed in the bottom at a depth of 14 m relative water-bottom interface (rhombus and triangle show positions of source and array, respectively). (b) Envelopes of received pulse on a logarithmic scale at a distance of 10,000 m from the source, at the point of the array location with and without taking into account horizontal refraction. (c, d) Pulse envelopes normalized by maximum value at a distance of 100 m and 10,000 m along the *x*-axis.

0.5 level increases by a factor of 1.5 times at a distance of 10 km, compared to the width at 100 m from the source.

8. Conclusions

Let us summarize the main features of low-frequency sound propagation in a shallow water waveguide, which are related to the details of the internal structure of the underlying half-space (seabed).

As follows from the results of three-dimensional engineering seismic surveys of the Arctic shelf, the ocean bottom has considerable inhomogeneities in its spatial structure. In terms of shallow water acoustics, these inhomogeneities manifest themselves in the form of complex spatial distributions of sound speed $c_1(x, y, z)$ in the bottom sediments.

The attenuation of the depth averaged intensity of the sound field for long-range propagation in such a waveguide is strongly dependent on the quantity $c_1(x, y, z)$, which is determined by, among other things, the extent to which the bottom sediments are saturated with gas. The sound wave attenuation coefficient in this case varies over a wide range: from a few tenths to ten dB km^{-1}. Such contrasts can be observed even for closely spaced acoustical tracks, including those emanating from the same point. For rather small but nonzero gas concentrations, a situation can be realized where the sound speed in the sea floor is close to that in the water. Such a sea bottom can be called water-like. For this type of bottom, the energy loses for waveguide sound propagation are maximal.

In addition to strong attenuation, effects of horizontal sound refraction can be manifested in the region of or close to the water-like bottom. This is possible even if the water surface and bottom are flat and the water layer is uniform. Horizontal refraction accompanies sound propagation along the boundary of the water-like bottom and is most pronounced at low frequencies, when only one mode propagates in the acoustical waveguide. Due to this effect, the sound intensity increases by 10 dB or more, and the sound pulse propagation time increases by 1.5%. The horizontal refraction angle may reach $\approx 10°$.

These features of low-frequency sound propagation are efficiently simulated in the framework of a modal sound field description. Coupling between modes should be considered at relatively high frequencies when sound waves propagate over the region of water-like sediments. The coupling has an almost negligible effect on the attenuation character of the depth averaged intensity of the sound field emitted by a point source. However, the mode coupling cause oscillations in the frequency dependence of the amplitudes of modes propagating over the water-like bottom. This fact can be used to localize such regions in experiments on stationary acoustical tracks. In regions where water-like sediments are absent, modal propagation can be treated as adiabatic (without coupling), and horizontal refraction can be disregarded (the uncoupled azimuth approximation is valid).

The material of this review can be useful for laying the physical foundations for acoustical monitoring of the Russian Arctic shelf. First and foremost, we mean monitoring aimed at large-scale acoustical thermometry of Arctic marginal seas [52] and at control of the level of anthropogenic noise that may affect protected marine mammals in this area.

References

1. Brekhovskikh L M, Lysanov Yu P *Fundamentals of Ocean Acoustics* (Modern Acoustics and Signal Processing) (New York: Springer, 2003) https://doi.org/10.1007/b97388; Translated from Russian: *Teoreticheskie Osnovy Akustiki Okeana* (Leningrad: Gidrometeoizdat, 1982); *Teoreticheskie Osnovy Akustiki Okeana* (Moscow: Nauka, 2007)
2. Katsnelson B G, Petnikov V G *Shallow Water Acoustics* (London: Springer, 2002); Translated from Russian: *Akustika Melkogo Morya* (Moscow: Nauka, 1997)
3. Pecknold S P, Masui K W, Hines P C *J. Acoust. Soc. Am.* **124** EL110 (2008)
4. Katsnelson B G et al. *Sov. Phys. Acoust.* **31** 321 (1985); *Akust. Zh.* **31** 537 (1985)
5. Otchet o 23-m reise NIS 'Akademik Kurchatov' (Report on the 23rd expedition of Research Vessel 'Akademik Kurchatov') (Moscow: Shirshov Institute of Oceanology of the Akad. Sci. of the USSR, 1976)
6. Knobles D P et al. *IEEE J. Ocean. Eng.* **35** 732 (2010)
7. Shakhova N et al. *Science* **327** 1246 (2010)
8. Kolyubakin A A et al. *Inzhenern. Izyskaniya* (10–11) 38 (2016)
9. Dmitrevskii N N et al. *Oceanology* **54** 116 (2014); *Okeanologiya* **54** 128 (2014)
10. Yashin D S, Kim B I *Geologiya Nefti i Gaza* (4) 25 (2007)
11. Homilton E L, in *Physics of Sound in Marine Sediments* (Marine Science, Vol. 1, Ed. L Hampton) (New York: Plenum Press, 1974); Translated into Russian: in *Akustika Morskikh Osadkov* (Ed. L Hampton, Russian Translation Ed. Yu Yu Zhitkovskii) (Moscow: Mir, 1977)
12. Belov A I, Kuznetsov G N *Acoust. Phys.* **59** 674 (2013); *Akust. Zh.* **59** 722 (2013)
13. Rutenko A N, Ushchipovskii V G *Acoust. Phys.* **61** 556 (2015); *Akust. Zh.* **61** 605 (2015)

14. Han D-G et al. *Front. Mar. Sci.* **10** 956323 (2023)
15. Ageeva N S et al. *Acoust. Phys.* **40** 159 (1994); *Akust. Zh.* **40** 181 (1994)
16. Belov A I, Zhuravlev V A, Komarov A G *Acoust. Phys.* **42** 290 (1996); *Akust. Zh.* **42** 334 (1996)
17. Belov A I, Komarov A G *Acoust. Phys.* **44** 260 (1998); *Akust. Zh.* **44** 312 (1998)
18. Boganik G N, Gurvich I I *Seismorazvedka* (Seismic Prospecting) (Tver: AIS, 2006)
19. Voskresenskii Yu N *Postroenie Seismicheskikh Izobrazhenii* (Construction of Seismic Profiles) (Moscow: RGU Nefti i Gaza, 2006)
20. Stepanov A V *Obrabotka Seismicheskikh Dannykh* (Processing of Seismic Data) (Kazan: Kazan. Univ., 2013)
21. Weinberg N L, Clark J G *J. Acoust. Soc. Am.* **68** 703 (1980)
22. Kravtsov Yu A, Kuz'kin V M, Petnikov V G *Sov. Phys. Acoust.* **30** 45 (1984); *Akust. Zh.* **30** 79 (1984)
23. Doolittle R, Tolstoy A, Buckingham M *J. Acoust. Soc. Am.* **83** 2117 (1988)
24. Shmelev A Yu, Migulin A A, Petnikov V G *J. Acoust. Soc. Am.* **92** 1003 (1992)
25. Badiey M et al. *J. Acoust. Soc. Am.* **117** 613 (2005)
26. Ballard M S, Lin Y-T, Lynch J F *J. Acoust. Soc. Am.* **131** 2587 (2012)
27. Grigor'ev V A, Petnikov V G, Roslyakov A G, Terekhina Ya E *Acoust. Phys.* **64** 331 (2018); *Akust. Zh.* **64** 342 (2018)
28. Petnikov V G, Grigorev V A, Lunkov A A, Sidorov D D *J. Acoust. Soc. Am.* **151** 2297 (2022)
29. Lunkov A, Sidorov D, Petnikov V *J. Mar. Sci. Eng.* **9** 1269 (2021)
30. Lunkov A A, Petnikov V G, Sidorov D D *Acoust. Phys.* **68** 357 (2022); *Akust. Zh.* **68** 400 (2022)
31. Sidorov D D, Petnikov V G, Lunkov A A *Acoust. Phys.* **69** 699 (2023); *Akust. Zh.* **69** 608 (2023)
32. Zhou J et al. *J. Acoust. Soc. Am.* **82** 2068 (1987)
33. Akal T, in *Physics of Sound in Marine Sediments* (Marine Science, Vol. 1, Ed. L Hampton) (New York: Plenum Press, 1974); Translated into Russian: in *Akustika Morskikh Osadkov* (Ed. L Hampton, Russian Translation Ed. Yu Yu Zhitkovskii) (Moscow: Mir, 1977)
34. Rozhin F V, Tonakanov O S *Obshchaya Gidroakustika* (General Acoustics) (Moscow: Izd. MGU, 1988)
35. Grigor'ev V A, Petnikov V G *Acoust. Phys.* **62** 700 (2016); *Akust. Zh.* **62** 681 (2016)
36. Grigoriev V A, Petnikov V G, Shatravin A V *Acoust. Phys.* **63** 433 (2017); *Akust. Zh.* **63** 389 (2017)
37. Katsnelson B, Petnikov V, Lynch J *Fundamentals of Shallow Water Acoustics* (New York: Springer, 2012)
38. Urick R J *Principles of Underwater Sound* (New York: McGraw-Hill, 1975); Translated into Russian: *Osnovy Gidroakustiki* (Library of the Acoustic Engineer) (Leningrad: Sudostroenie, 1978)
39. Grigor'ev V A, Lun'kov A A, Petnikov V G *Acoust. Phys.* **61** 85 (2015); *Akust. Zh.* **61** 90 (2015)
40. Brekhovskikh L M, Godin O A *Akustika Neodnorodnykh Sred* (Acoustics of Heterogeneous Media) Vol. 2 (Moscow: Nauka, 2009)
41. Grigor'ev V A, Lunkov A A, Petnikov V G *Phys. Wave Phenom.* **28** 255 (2020)
42. Collins M D *J. Acoust. Soc. Am.* **94** 2269 (1993)
43. Collins M D *J. Acoust. Soc. Am.* **96** 382 (1994)
44. Rutenko A N et al. *Acoust. Phys.* **58** 210 (2012); *Akust. Zh.* **58** 240 (2012)
45. Volkov M V et al. *Acoust. Phys.* **64** 692 (2018); *Akust. Zh.* **64** 676 (2018)
46. Uzhansky E et al. *J. Mar. Sci. Eng.* **9** 1423 (2021)
47. Rutenko A N et al. *Acoust. Phys.* **58** 326 (2012); *Akust. Zh.* **58** 356 (2012)
48. Sturm F *J. Acoust. Soc. Am.* **117** 1058 (2005)
49. Lin Y-T et al. *J. Acoust. Soc. Am.* **145** EL335 (2019)
50. Lunkov A A, Shermeneva M A *Acoust. Phys.* **68** 467 (2022); *Akust. Zh.* **68** 510 (2022)
51. Grigorev V A, Lunkov A A *Acoust. Phys.* **69** 525 (2023); *Akust. Zh.* **69** 453 (2023)
52. Munk W, Wunsch C *Deep Sea Res. A* **26** 123 (1979)
53. Grigorev V A *Acoust. Phys.* **68** 251 (2022); *Akust. Zh.* **68** 288 (2022)
54. DeSanto J A, in *Ocean Acoustics* (Topics in Current Physics, Vol. 8, Ed. J A DeSanto) (Berlin: Springer-Verlag, 1979); Translated into Russian: in *Akustika Okeana* (Ed. J A DeSanto, Russian Translation Ed. Yu A Kravtsov) (Moscow: Mir, 1982)
55. Brekhovskikh L M *Waves in Layered Media* (New York: Academic Press, 1980); Translated from Russian: *Volny v Sloistykh Sredakh* (Moscow: Nauka, 1973)
56. Gulin O E, Yaroshchuk I O *Acoust. Phys.* **64** 186 (2018); *Akust. Zh.* **64** 186 (2018)